Chemical properties, sources and size-resolved hygroscopicity of submicron black carbon-containing aerosols in urban Shanghai

Shijie Cui[1], Dan Dan Huang[2], Yangzhou Wu[1,a], Junfeng Wang[1], Fuzhen Shen[1,b], Jiukun Xian[1], Yunjiang Zhang[1], Hongli Wang[2], Cheng Huang[2], Hong Liao[1], Xinlei Ge[1, *]

[1] Jiangsu Key Laboratory of Atmospheric Environment Monitoring and Pollution Control, Collaborative Innovation Center of Atmospheric Environment and Equipment Technology, School of Environmental Science and Engineering, Nanjing University of Information Science and Technology, Nanjing 210044, China

[2] Shanghai Academy of Environmental Sciences, Shanghai 200233, China

[a]now at: Department of Atmospheric Sciences, School of Earth Sciences, Zhejiang University, Hangzhou 310027, PR China

[b]now at: Department of Meteorology, University of Reading, Reading, RG6 6BX, UK

*Corresponding author: Xinlei Ge (Email: caxinra@163.com)

For *Atmospheric Chemistry and Physics*

Abstract. Refractory black carbon (rBC) aerosols play an important role in air quality and climate change, yet high time-resolved and detailed investigation on the physicochemical properties of rBC and its associated coating is still scarce. In this work, we used a laser-only Aerodyne soot particle aerosol mass spectrometer (SP-AMS) to exclusively measure the rBC-containing (rBCc) particles, and compared their properties with the total non-refractory submicron particles (NR-PM$_1$) measured in parallel by a high-resolution AMS (HR-AMS) in Shanghai. The observation shows that rBC was overall thickly coated with an average mass ratio of coating to rBC core (R_{BC}) of ~5.0 (±1.7). However, mass of rBC coating species only occupied 19.1 (± 4.9)% of those in NR-PM$_1$; sulfate tended to condense preferentially on non-rBC particles therefore its portion on rBC was only 7.4 (± 2.2)%, while the majority of primary organic aerosols (POA) were associated with rBC (72.7 ± 21.0%). Positive matrix factorization reveals that cooking emitted organics did not coat on rBC, and a portion of organics coated on rBC was from biomass burning which was unidentifiable in NR-PM$_1$. Small rBCc particles were predominantly from traffic, while large-sized ones were often mixed with secondary components and typically had thick coating. Sulfate and secondary organic aerosol (SOA) species were generated mainly through daytime photochemical oxidation (SOA formation likely involved with in-situ chemical conversion of traffic-related POA to SOA), while nocturnal heterogeneous formation was dominant for nitrate; we also estimated the average time of 5~19 hours for those secondary species to coat on rBC. Particles during a short period that was affected by ship emissions, were characterized with a high vanadium concentration (on average 6.3 ± 3.1 ng m^{-3}) and a mean vanadium/nickel mass ratio of 2.0 (± 0.6). Furthermore, the size-resolved hygroscopicity parameter (κ_{rBCc}) of rBCc particles was obtained based on its fully chemical characterization, and was parameterized as $\kappa_{rBCc}(x)= 0.29-0.14 \times \exp(-0.006 \times x)$ (x is from 150 to 1000 nm). Under critical supersaturations (SS_C) of 0.1% and 0.2%, the D_{50} values were 166 (± 16) and 110 (± 5) nm, respectively, and with 16 (± 3)% and 59 (± 4))% of rBCc in number could be activated into cloud condensation nuclei (CCN). Our findings are valuable to advance the understanding of BC chemistry as well as the effective control of atmospheric BC pollution.

1 Introduction

Refractory black carbon (rBC) aerosols can directly absorb solar radiation, indirectly change the nature of cloud and alter the albedo of snow or glaciers (Jacobi et al., 2015), resulting in a positive radiative forcing that is second only to carbon dioxide on both regional and global scales (Ramanathan and Carmichael, 2008;Bond et al., 2013). The fresh rBC particles produced by incomplete combustion of biomass and fossil fuel tend to be fractal in morphology and can mix with many other components (Peng et al., 2016;Li et al., 2021). After entering into the atmosphere, fresh rBC can further externally or internally mix with organic/inorganic species which are primarily emitted or secondarily formed, and such aged rBC-containing (rBCc) particles (Chen et al., 2017;Lee et al., 2017) might have contrasting chemical properties and morphologies (or mixing states) (Liu et al., 2017a;Lee et al., 2019;Xie et al., 2019). In addition, when rBC mixes with hydrophilic materials, its hygroscopicity, cloud condensation nuclei (CCN) activity and size distribution, etc., can be significantly changed, which subsquently affect its atmospheric behavior, impact and lifecycle (Liu et al., 2013;Lambe et al., 2015). Therefore, it is necessary to elucidate the physicochemical characteristics and sources of rBC cores and associated coating materials, so as to better understand their influences on climate and air quality.

Chemical composition of ambient rBCc particles is largely dependent upon atmospheric conditions and emission sources. In general, the thickness of coating, mass contribution of secondary components (such as sulfate, nitrate and secondary organic aerosol (SOA) species) and oxidation degree of the coated organics of rBCc particles, increase with the aging time or oxidation capacity of ambient environment (Cappa et al., 2012;Liu et al., 2015;Wang et al., 2017;Collier et al., 2018;Wang et al., 2019), except in some specific cases that thickly coated rBCc might be dominated by primarily emitted particles (such as from biomass burning (Wang et al., 2017)). Recent field observations report that SOA species coated on rBC cores could account for 35% and 41% of the total SOA mass near traffic emission sources and in a polluted offshore environment, respectively (Massoli et al., 2012;Massoli et al., 2015). A study of rBCc particles in Singapore finds that over 90% of rBC derived from local combustion

80 sources (mainly traffic), while 30% of rBC was associated with fresh SOA generated

81 under the influences of daytime shipping and industrial emissions (Rivellini et al.,

82 2020).The SOA material concentrated on the surface of rBC was found to be chemically

83 different from the SOA that was externally mixed with rBC (Lee et al., 2017) in Fontana,

84 California, and another study in Shenzhen, China, reveals that more oxidized SOA

85 preferred to mix with rBC due to that abundant transition metals detected on rBC cores

86 might act as catalysts to convert less oxidized SOA to more oxidized SOA in aerosol

87 aqueous phase (Cao et al., 2022); the rBC could catalyze SO_2 to form sulfate as well,

88 as observed in Beijing (Zhang et al., 2020) and Guangzhou (Zhang et al., 2021), China.

89 Besides SOA, cooking-related OA is found to be externally mixed with rBC (Lee et al.,

90 2017;Wang et al., 2019), and a unique biomass burning related OA factor was identified

91 and was only present in rBCc rather than non-rBC particles during summertime in

92 Beijing (Wang et al., 2020a).

93   Size distribution of rBCc particles is also modulated greatly by their original

94 sources and ageing processes. For example, a study in Shanghai shows a bimodal size

95 distribution of rBCc, with a condensation mode dominated by traffic emissions (small

96 core size, thin coating) and a droplet mode including highly aged biomass burning

97 particles (large core size and thick coating) and highly aged traffic particles (small core

98 size and very thick coating) (Gong et al., 2016). Another study in Beijing (Liu et al.,

99 2019) further resolves four size modes of rBCc, relevant with traffic (small core, thin

100 coating), coal or biomass burning (moderate coating, both small and large cores), coal

101 combustion (large core, think coating) and secondary process (thick coating, both small

102 and large cores).

103   Moreover, water uptake and CCN activity of rBCc particles can increase with the

104 encapsulation of water-soluble substances such as sulfate, nitrate, and SOA (Liu et al.,

105 2013;Wu et al., 2019). Based on the measured chemical composition of rBCc, our

106 previous work has established a method for calculating size-resolved hygroscopicity

107 parameters of rBCc ($\kappa_{r\text{BCc}}$), and determined the CCN activation diameters of rBC

108 particles for given critical supersaturation (SS_C) values (Wu et al., 2019).

109   Highly time-resolved chemical characterization of rBCc particles were seldom

110 reported in China and is still lacking in Shanghai. In this study, we utilized an Aerodyne

111 soot particle aerosol mass spectrometer (SP-AMS) to determine the concentration,

112 composition and size distribution of rBCc particles exclusively (technical details in

113 Section 2.1) in urban Shanghai for the first time. We also compared the SP-AMS

114 measurement results with those from a co-located Aerodyne high-resolution time-of-

115 flight aerosol mass spectrometer (HR-AMS), to comprehensively investigate the

116 characteristics of rBCc particles. We analyzed $\kappa_{r\text{BCc}}$ and estimated the proportions of

117 activated rBCc numbers at given SS_C as well.

118

119 **2 Experimental methods**

120 **2.1 Sampling site and instrumentation**

121   The field measurement was conducted from October 31 to December 2, 2018,

122 during which the instruments were deployed on 8th floor of the building of Shanghai

123 Academy of Environmental Sciences (SAES) (31°10'33.348" N, 121°26'10.978" E).

124 Shanghai can be a representative of the densely populated megacity across the world;

125 the measurement period also belonged to the cold season when sources of rBCc might

126 be complex, and can offer rich information about the rBCc; of course, future

127 measurements in other seasons are still essential to achieve a complete understanding

128 of rBCc. East of the sampling site is a large commercial shopping center, and the site

129 is surrounded by residential areas with two busy arterial roads directly to the east (~450

130 m) and south (~150 m), respectively (Figure S1 in the supporting information). In

131 addition, the adjacent areas are densely populated with roadside residents, office

132 workers, and market traders, as well as crowds in and out of the Caobao Road Metro

133 station (~100 m). The measurement period was dominated by northeasterly winds,

134 while many international freight companies located on northeastern side of the site, and

135 many freighters were reposing on the Huangpu River. Overall, the sampling site was

136 probably influenced by vehicular emissions, residential activities and the northeast

137 Cargo ship emission plumes, etc.

138   An Aerodyne SP-AMS and an HR-AMS were operated in parallel during the

139 campaign. The two AMSs shared a same sampling line with a PM$_{2.5}$ cyclone (Model

140   URG-2000-30EN) in front to remove coarse particles. Ambient air pulled through the

141   sampling line was dried using a diffusion dryer filled with silicon gel and was

142   subsequently drawn into both instruments. Due to the transmission efficiency of the

143   inlet lens, both AMSs measured mainly particles of 30-1200 nm (denoted as PM_1).

144   The working principle of SP-AMS has been described in detail previously (Onasch

145   et al., 2012). However, in this work, we used only the intracavity infrared laser

146   vaporizer to selectively measure rBCc particles (rBC cores and associated coating

147   materials), as rBC can absorb 1064 nm laser light. The thermal tungsten vaporizer had

148   to be physically detached otherwise non-rBC particles can still be detected as the

149   filament can heat the vaporizer to ~200 $^\circ$C even if it was turned off. Before sampling,

150   the SP-AMS was tuned and calibrated following the steps described previously (Lee et

151   al., 2015;Willis et al., 2016;Wang et al., 2017). During sampling, due to relatively low

152   rBCc mass loadings, the SP-AMS was operated with two mass sensitive V modes (2.5

153   minutes per cycle), one with a particle time-of-flight (PToF) mode (30 s) and another

154   one (120 s) with a mass spectral mode with mass-to-charge (m/z) ratio up to 500.

155   Filtered air was also measured in the middle of campaign (for 60 min) to determine the

156   limits of detection (LOD, three times the standard deviation) of various aerosol species

157   and to adjust the air-influenced mass spectral signals (Zhang et al., 2005).

158   Before removal of the tungsten heater, the calibrations of ionization efficiency (IE)

159   for nitrate and relative ionization efficiency (RIE) of sulfate were performed by using

160   pure ammonium nitrate and ammonium sulfate particles (Jayne et al., 2000), and the

161   values were assumed to be unchanged throughout the whole campaign (Willis et al.,

162   2016). RIE of rBC to nitrate was calibrated by using size-selected (300 nm) BC

163   particles (REGAL 400R pigment black, Cabot Corp.) (Onasch et al., 2012), and the

164   average ratio of C_1^+ to C_3^+ was calculated to be 0.584 to correct the interference on C_1^+

165   from other organics. RIEs of ammonium, nitrate, sulfate and rBC were determined to

166   be 4.53, 1.10, 1.01, and 0.17, respectively, and RIE of organics used the default value

167   of 1.4 (Canagaratna et al., 2007). The size was calibrated by Polystyrene latex (PSL)

168   spheres (100–700 nm) (Duke Scientific Corp., Palo Alto, CA) before the measurement.

169   This study applied a collection efficiency (CE) of 0.5 for SP-AMS.

170   The co-located HR-AMS (DeCarlo et al., 2006) was used to measure all PM_1

171   including both rBCc and non-rBC particles, but it detected only non-refractory species

172   (NR-PM_1 species) as its 600 $^{\circ}$C thermal heater is unable to vaporize rBC and other

173   refractory components. In addition, mass concentrations of gaseous pollutants, carbon

174   monoxide (CO), ozone (O_3), nitrogen dioxide (NO_2), and sulfur dioxide (SO_2) were

175   measured by the Thermo Scientific analyzers provided by SAES. Meteorological

176   parameters including air temperature (T), relative humidity (RH), wind speed (WS),

177   wind direction (WD) and precipitation, were obtained from Xujiahui Environmental

178   Monitoring Station of Shanghai (31°11'49.1424"N, 121°26'34.44" E)(~2400 m away

179   from the site). The concentrations of particle-phase vanadium (V) and nickel (Ni) that

180   were used to investigate ship influence were measured independently by an

181   Atmospheric heavy metal analyzer (XHAM-2000A, SAIL HERO., China).

182

183   **2.2 Data analysis**

184   The AMS data (both SP-AMS and HR-AMS) were analyzed using standard ToF-

185   AMS data analysis tool (Squirrel version 1.59D and Pika version 1.19D), based on Igor

186   Pro 6.37 (Wavemetrics, Lake Oswego, OR, USA). The mass concentrations and high

187   resolution mass spectra (HRMS) of rBC and coating species (rBC_{CT}) were calculated

188   from high-resolution (HR) fitting of V-mode data. Size distributions of rBCc

189   components were determined by the PToF data with unit mass resolution and were

190   scaled to their mass concentrations obtained above. In particular, size distribution of

191   rBC was scaled to that of m/z 24 (C_2^+) (the scaling factor is rBC mass concentration to

192   that of calculated based on its size distribution), because m/z 24 as a rBC fragment, has

193   least interference from other organic or inorganic species; such treatment was adopted

194   in earlier studies too (Collier et al., 2018;Wang et al., 2019;Wang et al., 2016).

195   The HR ion fitting of AMS data is able to distinguish various ions and isotopic

196   ions and calculate elemental ratios of organics such as oxygen-to-carbon (O/C),

197   hydrogen-to-carbon (H/C), nitrogen-to-carbon (N/C), and organic mass to organic

198   carbon (OM/OC) ratios, via the original Aiken-ambient (A-A) method (Aiken et al.,

199   2008) and the improved method (I-A) (Canagaratna et al., 2015b). Outcomes of both

methods correlated well. Average O/C, H/C, and OM/OC ratios from the I-A method used in this work were 24.9%, 7.3%, and 5.6%, respectively, higher than those from the A-A method.

Furthermore, we performed Positive matrix factorization (PMF) (Paatero and Tapper, 1994) analysis on the HRMS of organics measured by the SP-AMS via the PMF Evaluation Tool (Ulbrich et al., 2009). The PMF solutions were thoroughly evaluated following the protocols documented in Zhang et al. (2011). Finally, a 6-factor solution was chosen as the optimal one. The final result included four primary OA (POA) factors, namely hydrocarbon-like species enriched OA (HOA-rich), rBC-enriched OA (rBC-rich), biomass burning OA (BBOA), water-soluble hydrocarbon-like species enriched OA (WS-HOA), and two secondary OA (SOA) factors including a less oxidized oxygenated OA (LO-OOA$_{r\text{BC}}$), and a more oxidized oxygenated OA (MO-OOA$_{r\text{BC}}$) (Key diagnostic plots in Fig. S2). As a comparison, the mass spectra of 5-factor and 7-factor solutions are illustrated in Fig. S3 (for the 5-factor solution, factor 3 is a mixed factor of BBOA and WS-HOA, while for the 7-factor solution, MO-OOA clearly splits into factor 5 and factor 2). The HR-AMS data were processed in a similar way, and four factors of NR-PM$_1$ organics were resolved, including hydrocarbon-related OA (HOA$_{\text{NR-PM1}}$), cooking OA (COA$_{\text{NR-PM1}}$), less oxidized oxygenated OA (LO-OOA$_{\text{NR-PM1}}$), and more oxidized oxygenated OA (MO-OOA$_{\text{NR-PM1}}$) (Mass spectra and time series shown in Fig. S4).

2.3 Calculation of size-resolved hygroscopicity of rBCc

The hygroscopicity parameter κ is a single parameter representing the hygroscopicity of particles, calculated based on essentially the chemical composition (Petters and Kreidenweis, 2007). SP-AMS measured size-resolved chemical compositions of rBCc can thus lead to size-resolved hygroscopicity of rBCc ($\kappa_{r\text{BCc}}$) (Wu et al., 2019;Hu et al., 2021). This study applied a similar method proposed by Wu et al. (2019) and the critical parameters involved in calculation are detailed in Table S1. The procedures are briefly described here: (1) obtain the matrice of size-resolved mass concentrations of each rBCc component from SP-AMS analysis; (2) convert the size-

230   resolved concentration matrice of inorganic ions (SO_4^{2-}, NO_3^- and NH_4^+) to

231   corresponding matrice of inorganic salts (NH$_4$NO$_3$, NH$_4$HSO$_4$, (NH$_4$)$_2$SO$_4$) using a

232   simplified solution of ion pairs (Gysel et al., 2007); (3) convert the size-resolved mass

233   matrice of all components (inorganic salts, OA and rBC) to those of size-resolved

234   volume fractions (Gysel et al., 2007;Chang et al., 2010;Wu et al., 2016); (4) combine

235   with previously reported hygroscopic parameters (Gysel et al., 2007;Chang et al.,

236   2010;Wu et al., 2016) to obtain the volumetric contributions of each component to the

237   hygroscopicity of rBCc; (5) use the Zdanovskii-Stokes-Robinson (ZSR) rule to derive

238   the size-resolved hygroscopicity of rBCc (κ_{rBCc}) (Topping et al., 2005b, a).

239

240   **3 Results and discussion**

241   **3.1 Overview of chemical characteristics of rBCc and NR-PM$_1$ particles**

242   Figure 1 presents the time series of meteorological parameters, concentrations of

243   gaseous pollutants (CO, NO$_2$, O$_3$, and SO$_2$), ship emission tracers (vanadium and

244   nickel), rBC and rBC$_{CT}$ species and their mass percentages to the total rBCc mass,

245   PMF-resolved OA factors and their corresponding fractional contributions. The

246   sampling period was featured by relatively moderate temperatures and very stagnant

247   conditions with average ($\pm 1\sigma$) temperature of 15.3 ($\pm$ 2.9) °C and wind speed (WS) of

248   0.16 ($\pm$ 0.29) m s^{-1}. The wind with speeds <0.5 m s^{-1} dominated most of the sampling

249   days and 42% of sampling time was with near-zero wind, therefore overall influence of

250   WS and WD on surface mass loadings of rBCc was insignificant. Yet one should keep

251   in mind that WD can affect rBCc sources, and WS in higher altitude might be stronger

252   therefore long-range transport of air pollutants was still possible. The average

253   concentrations of CO, NO$_2$, O$_3$, SO$_2$, V, and Ni were determined to be 0.60 ($\pm$ 0.26)

254   ppm, 29.20 ($\pm$ 17.07) ppt, 27.10 ($\pm$ 15.97) ppt, 1.27 ($\pm$ 0.72) ppt, 4.05 ($\pm$ 3.19) ng m^{-3},

255   and 3.06 ($\pm$ 2.45) ng m^{-3}, respectively.

256   The mass loadings of rBC and rBC$_{CT}$ ranged from 0.04 to 11.00 μg m^{-3} and 0.37

257   to 30.47 μg m^{-3} with campaign-mean values ($\pm$ 1σ) of 0.92 ($\pm$ 0.81) μg m^{-3} and 4.55 ($\pm$

258   4.40) μg m^{-3}. The coating materials accounted for 81.8 ($\pm$ 5.3)% of the total rBCc mass,

259   of which organics was the most abundant species (2.54 $\pm$ 2.52 μg m^{-3}, 46.6 $\pm$ 6.4%),

260   followed by nitrate (1.20 ± 1.30 µg m^{-3}, 18.5 ± 8.0%), ammonium (0.44 ± 0.40 µg m^{-3},

261   8.0 ± 2.0%), sulfate (0.30 ± 0.19 µg m^{-3}, 7.1 ± 3.6%), and chloride (0.07 ± 0.05 µg m^{-3},

262   1.7 ± 1.0%). The mass ratio of rBC$_{CT}$ to rBC (R_{BC}) ranged from 2.2 to 9.0, with an

263   average of ~5.0 (± 1.7). The average R_{BC} was higher than that in California ($R_{BC} = 2.3$)

264   (Collier et al., 2018) and in Shenzhen ($R_{BC} = 2.5$)(Cao et al., 2022), lower than that in

265   Tibetan Plateau ($R_{BC}=7.7$) (Wang et al., 2017) and similar to that in Beijing ($R_{BC}=5.0$)

266   (Wang et al., 2019), suggesting rBC was relatively thickly coated throughout the

267   campaign. Correlation between rBC and rBC$_{CT}$ was moderate (Pearson's $r = 0.76$).

268   Correlation coefficients (r) of chloride, nitrate, sulfate and organics with rBC were 0.72,

269   0.87, 0.71 and 0.73, respectively, suggesting variability of sources among different

270   coating components.

271   Figure 2 compares the campaign-averaged diurnal patterns of rBC$_C$ and NR-PM$_1$

272   species, chemical compositions of rBCc and NR-PM$_1$, and mass ratios of the species

273   coated on rBC to those of NR-PM$_1$. We found that the diurnal variations of nitrate,

274   sulfate, ammonium, chloride were very similar ($r > 0.92$) between the two particle

275   groups, while apparent difference was found for rBCc organics with a much obvious

276   morning rush hour peak (6:00 - 9:00). The results indicate that the formation processes

277   of inorganic salts coated on rBC were similar to those uncoated on rBC, but there were

278   large difference regarding sources/processes existed for organics. For rBC itself, the

279   diurnal cycle presented clearly a morning peak and an evening peak, likely relevant

280   with rush hour traffic emissions (CO showed similar pattern). On the contrary, R_{BC} had

281   a minimum in the morning and dropped to a low level in later afternoon, probably due

282   to influence from traffic-emitted fresh and barely coated rBC particles (details in

283   Section 3.2.1).

284   Distributions of species between rBCc and non-rBC particles were also different,

285   leading to different chemical compositions (Figs. 2g and 2h). Sulfate tended to

286   preferentially condense on non-rBC particles, as its mass contribution to total rBCc

287   mass was only $6.5 (\pm 4.2)$%, while its contribution to total NR-PM$_1$ was $17.6 (\pm 8.3)$%.

288   Apportionment of nitrate between rBCc and non-rBC particles was about even as it

289   both occupied ~26% of the total rBCc and NR-PM$_1$ masses. Organics occupied 55.9 ($\pm$

290 9.2)% of rBCc mass, larger than it in NR-PM$_1$ (43.7 ± 11.7%), due to that primary OA

291 species preferentially associated with rBC. Such result is similar to that observed in

292 winter in Beijing but contrary to the result that SOA was more abundant in rBCc in

293 Shenzhen (Cao et al., 2022).

294   On average, rBC$_C$ accounted for 19.1% of the total NR-PM$_1$ mass loading (21.61

295 ± 15.80 μg m^{-3})(Fig. 2i), comparable to that in Fontana, California (Lee et al., 2017).

296 The finding reveals that significant fractions of aerosol species were externally mixed

297 with rBC. Individually, sulfate captured by rBC only represented 7.4 (± 2.2)% of NR-

298 PM$_1$ sulfate, similar to the earlier results (Lee et al., 2017;Wang et al., 2020a;Cao et al.,

299 2022;Ma et al., 2020); mass fractions of rBCc nitrate (20.1 ± 5.2%) and chloride (20.4

300 ± 5.5%) in NR-PM$_1$ were similar to the portion of total rBC$_C$ (19.1 ± 4.9%), while the

301 fraction of organics was higher (26.1 ± 7.3%). The lower fraction of sulfate in rBCc

302 than nitrate was likely due to a few reasons. One probable reason is traffic was a

303 dominant source of rBC (see Section 3.2.1 for details) and NO$_2$ is known to be mainly

304 from traffic as well, therefore secondarily formed nitrate was easy to condense on co-

305 emitted rBC, however SO$_2$ is mainly from other sources rather than traffic. Another

306 possible cause is that rBC concentration was relatively high during nighttime, and

307 nighttime formation of nitrate was significant; Sulfate, on the other hand, was mostly

308 formed in the afternoon due to photochemical oxidation in this study (see Section 3.3.2

309 for details), whereas afternoon rBC concentration was low. The relatively high ratio of

310 organics was attributed to the fact that majority of POA species were coated on rBC

311 (average ratio of 72.7 ± 21.0%), while rBC-related SOA was 21.8 (± 7.7)% of the total.

312 Note the rBCc POA here included all four POA factors, and COA$_{NR-PM1}$ did not coat on

313 rBC thus was not included in the calculation.

314

315   **3.2 Distinctive sources of OA in rBCc and in NR-PM$_1$**

316   As shown previously, source apportionment results of OA in rBCc and NR-PM$_1$

317 were different. This section discusses in details the characteristics of OA sources in

318 rBCc and in bulk NR-PM$_1$.

3.2.1 Source apportionment of OA in rBCc

Figure 3 shows the HRMS and temporal variations of the six OA factors resolved from PMF analysis of rBCc organics. Note the PMF analysis included rBC signals (i.e., C_x^+ ions) to aid identification of different factors, yet calculations of elemental ratios of these OA factors did not include C_x^+ ions in order to explicitly explore the properties of organic coating. The HRMS of HOA-rich and rBC-rich were similar to the OA previously reported in urban environments near traffic emissions and/or in gasoline/diesel vehicle exhaust (Massoli et al., 2012;Lee et al., 2015;Enroth et al., 2016;Saarikoski et al., 2016;Willis et al., 2016;Lee et al., 2017), therefore both factors were traffic-related. The HOA-rich mass spectrum was featured by intense hydrocarbon ion series (i.e., $C_nH_{2n+1}^+$ and $C_nH_{2n-1}^+$ ions in Fig. 3c), and a lowest O/C ratio of 0.07. Mass fraction of rBC signals (i.e., C_n^+ ions, such as m/z 12, 24, 36, 48, and 60, etc.) in HOA-rich was 8.1%. Mass spectrum of rBC-rich factor had remarkable contribution from rBC (24.2%). Beside C_n^+ ions, the rBC-rich factor contained more oxygenated organic fragments and presented a higher O/C ratio of 0.21 than that of HOA-rich, similar to previous studies (Willis et al., 2016;Lee et al., 2017). This result is reasonable as previous studies (Corbin et al., 2014;Malmborg et al., 2017) found that refractory organics could generate oxygenated ion fragments (such as CO^+ and CO_2^+ derived from oxygenated species on soot surface or inside soot nanostructure). HOA-rich factor correlated very well with the common AMS tracer of vehicular OA, $C_4H_9^+$ (r=0.95, Fig. 3i), while rBC-rich factor did match the variation of rBC well (r=0.90, Fig. 3g). Since diesel combustion often releases more rBC than that of gasoline, it is likely that the rBC-rich factor is representative of diesel vehicle exhaust while HOA-rich factor represents gasoline combustion emissions. This result demonstrates that laser-only SP-AMS is capable of distinguishing diesel and gasoline burning particles which typically cannot be separated by other AMS measurements. Further verification should be subject of future work.

In this work, a multiple linear regression for the three-dimension size-resolved mass spectra according to the method provided in Ulbrich et al. (2012) was used to resolve the average size distributions of six OA factors. The diagnostic plots are shown

349 in Fig. S5. Overall, the lumped size distribution of six OA factor could reproduce well

350 that of total OA (except for a few size bins, most deviations are within 10%).

351 Correlation between measured and reconstructed OA of all size bins was very tight with

352 r of 0.99 and a slope of 0.97, indicating the robustness of the regressed size distributions

353 of all OA factors. The results together with size distributions of rBCc components, and

354 corresponding mass fractional contributions of different components in all size bins are

355 illustrated in Fig. 4. The average HOA-rich size distribution peaked around 150 nm

356 (D_{va}, vacuum aerodynamic diameter), generally matching with previously reported size

357 distribution of HOA (Sun et al., 2012;Ulbrich et al., 2012;Zhou et al., 2016).

358 Interestingly, size distribution of rBC-rich factor presented two modes, with one

359 peaking ~260 nm, and a more pronounced one peaking ~580 nm (Fig. 4a).

360   The BBOA was identified owing to its obviously higher signals of $C_2H_4O_2^+$ (2.03%)

361 and $C_3H_5O_2^+$ (1.62%) than those in other factors, as these two ions are well-known AMS

362 fragments of the biomass burning tracer, levoglucosan (Mohr et al., 2009;Cubison et

363 al., 2011). The time series of BBOA correlated particularly tightly with both marker

364 ions (r of 0.86 and 0.80, respectively); it in fact also correlated well with K^+ (r=0.79),

365 another tracer of biomass burning emission. The O/C and H/C ratios of BBOA were

366 0.12 and 1.78, and C_n^+ ions accounted for 9.1% of BBOA, all suggesting that the factor

367 was fresh and might be co-emitted with rBC. A relatively high N/C ratio (0.033) was

368 found for BBOA, which could be attributed to the large amounts of nitrogen-containing

369 organic species enriched in biomass burning OA (Laskin et al., 2009). In addition, the

370 size distribution of BBOA (Fig. 4a) (peak size ~500 nm) was similar to that of biomass

371 burning BC-containing particles obtained using single particle mass spectrometry in

372 Shanghai (Gong et al., 2016).

373   The PMF analysis deconvoluted a unique OA factor coated on rBC, namely WS-

374 HOA. Firstly, the WS-HOA mass spectrum had a series of hydrocarbon ion fragments

375 and its time series correlated well with them (e.g., r of 0.90 and 0.92 for WS-HOA $vs.$

376 $C_4H_7^+$ and $C_4H_9^+$, respectively). Secondly, this factor correlated the best (r=0.57) with

377 aerosol liquid water content (ALWC) (Fig. 3j) compared with the other five OA factors

378 (all r<0.2). Thirdly, a previous study (Ye et al., 2017) that investigated specially the

water-soluble fraction of OA via PMF analysis, separated also a HOA factor that contained significant nitrogen-containing organic fragments, with a highest N/C ratio among all other factors, and correlated well those nitrogenated fragments. The WS-HOA defined here showed similar characteristics with the highest N/C (0.037) among all factors and tight correlations with nitrogen-containing fragments ($r>0.80$). At last, although WS-HOA had a relatively high O/C (0.31) with remarkable contributions from $C_2H_3O^+$ and CO_2^+, yet its correlations with these two ions were in fact not strong (r of 0.46 and 0.44, respectively); and WS-HOA had the least fraction of rBC fragments (0.9%) (note rBC is hydrophobic), even less than the two SOAs (Fig. 3d). Both results suggest that this factor is a collection of water-soluble primary OA species. The peak of WS-HOA size distribution was ~150 nm, close to that of HOA-rich (Fig. 4a). Aqueous-phase processed SOA (aqSOA) were typically with very high O/C ratio (Xu et al., 2019), and size distribution of aqSOA often presented a droplet mode, peaking in relatively large sizes (such as 500~600 nm)(Gilardoni et al., 2016;Wang et al., 2021;Ge et al., 2012). Therefore, the moderate O/C (0.31) and small mode size of WS-HOA again manifest it was not from aqueous-phase reactions but more likely the water-soluble fraction of POA.

The PMF analyses separated two SOA factors, LO-OOA$_{r\text{BC}}$ and MO-OOA$_{r\text{BC}}$. Mass spectral features of the two SOAs were consistent with previous studies: The LO-OOA$_{r\text{BC}}$ was rich in $C_xH_yO_1^+$ ions (38.7%) (such as $C_2H_3O^+$ at m/z 43) but with less contribution from $C_xH_yO_2^+$ ions (7.6%) and an overall moderate O/C (0.25), while MO-OOA$_{r\text{BC}}$ had much more contribution from $C_xH_yO_2^+$ ion family (22.7%) (such as CO_2^+ at m/z 44) and $C_xH_yO_1^+$ ions (44.7%), with a high O/C ratio (0.56). In addition, LO-OOA$_{r\text{BC}}$ correlated better with nitrate ($r=0.83$) than it with sulfate ($r=0.69$), while the correlation between MO-OOA$_{r\text{BC}}$ and sulfate ($r=0.84$) is better than it with nitrate ($r=0.76$). Size distributions of the two SOAs were also in accord with their secondary behaviors, both accumulating at larger sizes (~450 nm for LO-OOA$_{r\text{BC}}$, and a bit larger mode size of ~500 nm for MO-OOA$_{r\text{BC}}$), in agreement with previous observations (Sun et al., 2012;Ulbrich et al., 2012;Zhou et al., 2016).

In total, traffic-related POA (sum of HOA-rich, rBC-rich and WS-HOA) was the

most abundant source of rBCc organics (39.1%); BBOA occupied ~18.4%; the contributions of two SOAs were on par with each other (20.2% for LO-OOA$_{r\text{BC}}$, and 22.3% for MO-OOA$_{r\text{BC}}$) (Fig. 2g). Among traffic POA, gasoline derived HOA-rich factor outweighed the diesel derived rBC-rich factor (11.4% $vs.$ 6.3% of the total rBCc). Contributions of different factors varied greatly for different sizes of rBCc particles (Fig. 4b). Small-sized particles were overwhelmingly dominated by traffic POA; SOA contributions increased with increase of size, and dominated over POA for 300-800 nm ones; contribution of BBOA was also relative larger for 300-800 nm than for other-sized ones; the very large particles (800-1000 nm) were found to be affected mainly by traffic POA in this work. Correspondingly, for the total rBCc particles, rBC cores peaked at ~170 nm, while other secondary inorganic components, behaving like SOA factors, all peaked at a big size (~550 nm) (Fig. 4c) and their mass percentages were also large for large-sized particles (Fig. 4d).

Figure 5a further demonstrates the changes of mass fractions of each rBCc component as a function of R_{BC}. R_{BC} is a proxy of coating thickness. It was found that the thinly coated rBCc ($R_{\text{BC}}<3$) were dominated (up to ~80%) by traffic-related POA. With the increase of R_{BC}, contribution of secondary components increased gradually, especially the two SOAs and nitrate (sulfate showed little changes across the whole R_{BC} range); SOA and nitrate contributions reached 40.2% and 31.3% at $R_{\text{BC}} = 8$, respectively. Accordingly, the oxidation degree (OSc = 2*O/C-H/C) (Kroll et al., 2011) of coated organics increased with R_{BC}. In Fig. 5b, we presented the mass contributions of OA factors to the rBC mass at different R_{BC} values. The rBC was as expected, predominantly associated with POA (from 94% at $R_{\text{BC}}<2$ to 66% at $R_{\text{BC}}>8$), similar to those from Fontana (Lee et al., 2017). Contribution of rBC-rich factor decreased obviously, and those of SOA factors increased with R_{BC}. The contributions of HOA-rich, WS-HOA and BBOA factors changed little.

3.2.2 Comparisons with NR-PM$_1$ organics

As shown in Fig. S4, PMF analysis separated four OA factor for NR-PM$_1$ organics. Two SOA factors (LO-OOA and MO-OOA) were resolved for both rBCc and NR-PM$_1$,

and their contributions to them were also close (Figs. 2g and 2h). Correlations of time series between the two LO-OOA factors and between the two MO-OOA factors were also tight (r of 0.94 and 0.90, respectively), indicating similar formation processes for each SOA. But, of course, the SOAs from rBCc and from NR-PM$_1$ were not entirely the same, as later ones had higher O/C ratios (0.52 of LO-OOA$_{NR-PM1}$ and 0.62 of MO-OOA$_{NR-PM1}$). On average, the portion of LO-OOA coated on rBC took up 21.6% mass of LO-OOA in total NR-PM$_1$, and the portion was 26.0% for MO-OOA. This result suggests that there were some differences regarding the partitioning of LO-OOA and MO-OOA onto rBCc and non-rBC particles.

Compared with SOAs, source apportionment results of POA were quite distinct. Firstly, there was only one HOA factor resolved for NR-PM$_1$, while three HOA factors were separated for rBCc. Note the rBC-rich and WS-HOA factors occupied merely 3.1% and 2.1% of NR-PM$_1$ OA mass, respectively, probably the cause that they were not identified in NR-PM$_1$ OA. Nevertheless, mass loadings of the sum of HOA-rich, rBC-rich and WS-HOA factors (termed as HOA$_{rBC}$) agreed quite well with that of HOA$_{NR-PM1}$ (r=0.95) (Fig. S7), verifying both source apportionment results. And, HOA$_{rBC}$ took up 63.7% of HOA$_{NR-PM1}$, while previous studies reported that 81% (Massoli et al., 2012) and 87 % (Massoli et al., 2015) of HOA were associated with rBC. These results imply that HOA species in NR-PM$_1$ were largely internally mixed with rBC affected by vehicular emissions. Secondly, COA$_{NR-PM1}$ was only identified in NR-PM$_1$ OA. AMS-resolved COA$_{NR-PM1}$ is mainly from cooking oil and food ingredients, therefore it negligibly internally mixes with rBC. This result is consistent with previous observations (Lee et al., 2015;Willis et al., 2016;Lee et al., 2017;Collier et al., 2018). At last, BBOA was identified in rBCc OA but not in NR-PM$_1$ OA. One plausible reason was that the BBOA mass contribution was minor (equivalent to <5% of NR-PM$_1$ OA mass) therefore was not able to be separated from other OA factors; another speculation is that laser only SP-AMS can detect refractory species that HR-AMS cannot, and a portion of these refractory species are likely rich in biomass burning OA. Identification of BBOA in rBCc rather than in simultaneously measured total NR-PM$_1$ was also found in Tibet (Wang et al., 2017) and Beijing (Wang et al., 2020a), role

469   of such BBOA and its interplay with rBC core remain a subject of future work.

470   Diurnal cycles of the POA and SOA factors from both PMF analyses are compared

471   in Figs. 6a and 6b. The diurnal pattern of stacked HOA$_{r\text{BC}}$ indeed agreed with that of

472   HOA$_{\text{NR-PM1}}$, both with two peaks in the morning and evening rush hours, and, the

473   patterns of rBC-rich, HOA-rich, and WS-HOA factors showed similar behaviors

474   individually (Fig. 6a). The diurnal variation of COA$_{\text{NR-PM1}}$ had pronounced peaks

475   during lunch and dinner times, and its percentage in NR-PM$_1$ OA reached 54% at night.

476   Diurnal patterns of two LO-OOA factors were somewhat different (r=0.35)(Fig. 6b).

477   LO-OOA$_{r\text{BC}}$ has a major peak in the afternoon, while though LO-OOA$_{\text{NR-PM1}}$

478   concentration rose in the afternoon too but peaked in early evening (~20:00). The daily

479   variations of two MO-OOA factors were similar (r=0.83), both peaking at 16:00. The

480   afternoon increases of both SOAs indicate an important role of photochemical reactions,

481   yet differences in formation mechanisms, volatilities and partitioning behaviors of SOA

482   products could lead to diversities of their diurnal patterns and HRMS.

483

484   **3.3 Evolution and formation rBCc components**

485   **3.3.1 Behaviors of rBC cores**

486   Size distribution of rBC cores shown in Fig. 4c was relatively wide. Beside the

487   main peak at ~170 nm, it extended significantly into large sizes and had a small peak at

488   ~550 nm, which was close to the peak of secondary components. With results shown in

489   Fig. 5a, we found that small rBC cores were often thinly coated, while thickly coated

490   rBCc particle were often highly aged and a portion of them also had large-sized rBC

491   cores. This result is likely owing to that oxidation of rBC-bounded organics and/or

492   condensation of secondary species onto rBC surface can induce restructuring of soot

493   aggregates to form compact and large cores (Chen et al., 2018;Chen et al., 2016). Such

494   phenomenon is in line with earlier studies (Liu et al., 2019;Gong et al., 2016). We

495   further show the image plot of size distributions of rBC at different R_{BC} in Fig. S8a. It

496   can be found that the rBC mass in a large part concentrated in particles with R_{BC} of 5-

497   8, and there was indeed a significant portion of rBC appearing in large size range (400-

498   800 nm) with very thick coating (R_{BC} of 8-9).

3.3.2 Formation of inorganic salts

Sulfate and nitrate both peaked at a big size ~550 nm (Fig. 4c) and were mainly associated with thickly coated rBCc (R_{BC}>6, Figs. S8d and S8e). To investigate the impacts of photochemistry and aqueous/heterogeneous chemistry on the formation of rBC$_{CT}$ species, we plotted the image plots of size distributions of nitrate, sulfate and organics versus O$_X$ (O$_3$ + NO$_2$) and relative humidity (RH) in Fig. 7. Here O$_X$ is used as a proxy of photochemical activity (Xu et al., 2017), and RH is an indicator of aqueous reactions (Wu et al., 2018). Nitrate significantly concentrated in 65-100 ppb O$_X$ range but there was a weak accumulation in low O$_X$ as well (Fig. 7a), while in Fig. 8d, nitrate had a prominent hotspot in RH>85%. Generally, both strong photochemical activity and high RH could promote nitrate formation. For sulfate, although the distribution was scattered due to low level of mass loadings, high Ox level seemed to favor sulfate formation (Fig. 7b); sulfate was scattered in the whole RH range and there were some enhancements at high RH (>80%) but was much less clear-cut (Fig. 7e). Therefore aqueous-phase production of sulfate was not important in this campaign.

We further calculated the sulfur oxidation ratio (SOR) and nitrogen oxidation ratio (NOR) (Xu et al., 2014), and plotted their variations against O$_X$ and RH in Figs. 8a and 8e, respectively. The NOR rose substantially at O$_X$ >60 ppb but showed no increase at O$_X$ < 60 ppb, while it increased continuously with RH. Mass ratio of nitrate to rBC stayed at a high level during nighttime when RH was high as well (overall diurnal trend of NO$_3^-$/rBC was similar to that of RH, see Figs. S9a and S9d). This result indicates a likely more important role of nocturnal nitrate formation (N$_2$O$_5$ hydrolysis) (Pathak et al., 2011) (Sun et al., 2011) than photochemical production of nitrate during this campaign; moreover, low temperature and high RH favor nitrate partitioning into the particle phase during nighttime too (Gao et al., 2011). For sulfate, The SOR increased with O$_X$ while it increased with RH under relatively dry conditions (<60%) but decreased with RH when RH>60%. This result, on the other hand, highlights that photochemical production is more important than aqueous/heterogenous formation for sulfate. In addition, mass ratios of sulfate to rBC were enhanced remarkably during daytime and peaked in the afternoon (Fig. S9e), supporting the key role of

529   photochemical formation of sulfate. Sulfate precursor SO_2 was at a high level during

530   daytime too. The main formation pathway of sulfate is strikingly different from that

531   observed in winter Nanjing (Wu et al., 2018), suggesting significant seasonal variability

532   of sulfate formation even in the same region.

533

534   **3.3.3 Evolution of organics**

535   Organics had a broad average size distribution (Fig. 4c), but unlike rBC, its main

536   peak appeared at 500~600 nm. Figure S8b shows that the majority of organics

537   partitioned in rBCc with R_{BC} of 5.0-9.0 and wide size coverage (300-800 nm).

538   Regarding its dependences on O_X and RH, it mainly accumulated at O_X>70 ppb (Fig.

539   7c) and very high RH (~90%) (Fig. 7f). Consistently, O/C ratio and OSc both peaked

540   in the afternoon (Fig. S9b), all suggesting a critical role of photochemistry in affecting

541   the behavior of organics.

542   Figure 8 illustrates the mass ratios of each OA factor to rBC varying with O_X and

543   RH. Mass ratios of all four POA factors generally presented decreasing trends (despite

544   some fluctuations) against O_X (Fig. 8b), and the total POA$_{rBC}$ showed evident decrease

545   with increase of O_X (Fig. 8d). Instead, both LO-OOA$_{rBC}$ and MO-OOA$_{rBC}$, as well as

546   their sum (SOA$_{rBC}$) increased continuously with O_X (Figs. 8c and 8d). This result proves

547   that photochemical oxidation contributed significantly to both LO-OOA$_{rBC}$ and MO-

548   OOA$_{rBC}$ formations. Comparatively, decreases of POA$_{rBC}$ perhaps point to its reaction

549   loss upon photochemical oxidation. With regard to RH, besides WS-HOA, the other

550   three POA$_{rBC}$ factors showed almost no dependences on RH (Fig. 8f); note the increase

551   of WS-HOA with RH did not indicate the aqueous production of WS-HOA (see

552   discussion in Section 3.2.1), but a result of enhanced dissolution with increase of

553   moisture. Overall small increase of POA$_{rBC}$ (Fig. 8h) with RH then mainly attributed to

554   WS-HOA. Contrary to the trends with O_X, mass ratios of two SOA factors as well as

555   the total SOA to rBC went down with increase of RH (Figs. 8g and 8h), indicating a

556   trivial role of aqueous/heterogenous oxidation for the SOA coated on rBC observed

557   during this campaign.

558   The aging of OA is generally characterized by the increase of O/C and decrease of

559 H/C (Ng et al., 2011;Zhao et al., 2019).The different aging pathways of OA follow

560 different slopes in the Van Krevelen (VK) diagram (Heald et al., 2010). For example,

561 addition of only one oxygen atom to the carbon skeleton results in a slope equal to 0,

562 while replacement of the hydrogen atom with a carboxylic acid group (−COOH) results

563 in a slope of −1 without fragmentation (C-C bond breaking), and −0.5 with

564 fragmentation (Heald et al., 2010;Ng et al., 2011;Zhao et al., 2019). As presented in Fig.

565 10a, fitting of all OA data yielded a slope of −0.96, very close to −1, suggesting that

566 OA ageing process resembled the hydrogen substitution with a –COOH group

567 (carboxylation). Interestingly, the four OA factors (HOA-rich, WS-HOA, LO-OOA$_{rBC}$

568 and MO-OOA$_{rBC}$) aligned almost in a straight line with a slope of −0.77 (Fig. 9a), also

569 close to −1. Figure S10 further reveals that there was a strong anti-correlation between

570 mass fractions of sum of HOA-rich and WS-HOA and sum of LO-OOA$_{rBC}$ and MO-

571 OOA$_{rBC}$ (r=−0.97); the slope of fitted line was −0.86. All these results suggest that OA

572 evolution may contain a channel of photochemical transformations from HOA-rich and

573 WS-HOA to LO-OOA$_{rBC}$ and then to MO-OOA$_{rBC}$. This result is also in line with the

574 observed decrease of POA$_{rBC}$ and increase of SOA$_{rBC}$ against O$_X$.

575   CHO$^+$, CHO$_2^+$ and C$_2$H$_2$O$_2^+$ are the AMS tracer ions for carbonyl, carboxylic acid

576 and glyoxal, respectively (Wang et al., 2020b;Canagaratna et al., 2015a;Yu et al., 2014).

577 Mass fractions of these three fragment ions presented decreasing trends (or no clear

578 trends) against RH (Fig. S11), suggesting again that aqueous processing is not an

579 important pathway in OA evolution during this campaign. Conversely, fractional

580 contributions of these three ions presented increasing trends versus O$_X$, supporting the

581 dominance of photochemical oxidation pathway (Figs. 9b-d). Figures 9e-g show the

582 scatter plots of H/C versus O/C at different O$_X$ concentrations. The regressed slope was

583 −1.03 for low O$_X$ (<60 ppb) conditions (Fig. 9e), indicating that the OA aging at low

584 O$_X$ level is mainly analogue to the carboxylation process. This result corresponds

585 precisely to the fact that mass fractions of CHO$_2^+$ and C$_2$H$_2$O$_2^+$ increased gradually with

586 O$_X$ at low O$_X$, whereas that of CHO$^+$ remained essentially unchanged (Figs. 9b-d). The

587 fitted slope was −1.14 for moderate O$_X$ conditions (60-80 ppb), and it changed to −0.43

588 for high O$_X$ level (>80 ppb) but correlation became weaker (r=−0.57). This result

589   implies that the OA evolution under high O_X conditions might include oxidations by

590   the additions of alcohols, peroxides and carboxylation. In all, the evolution of rBCc OA

591   in Shanghai during this campaign is governed by photochemistry rather than aqueous

592   chemistry, but with different oxidation pathways at different O_X levels.

593

594   **3.3.4 Coating time of secondary species onto rBC**

595   Although the rBCc organics was dominated by primary sources (Fig. 2g), the

596   diurnal variations of OSc, O/C and H/C of the total organics, were controlled

597   predominantly by the two SOA factors. Correlations between the diurnal cycles of MO-

598   OOA$_{rBC}$/rBC and OSc were extremely well (r=0.97 with OS_C and r=0.98 with O/C),

599   and those of LO-OOA/rBC were also tight (r=0.91 with OS_C and r=0.92 with O/C).

600   The correlations with LO-OOA$_{rBC}$ were a bit weaker than those of MO-OOA$_{rBC}$,

601   indicating that MO-OOA$_{rBC}$ was probably the final products and was more important

602   in governing the overall oxidation level of organic coating. Figure 10a depicts the

603   diurnal variations of SOA$_{rBC}$/rBC and POA$_{rBC}$/rBC. Diurnal variations of POA$_{rBC}$/rBC

604   and rBC were overall similar, while the daily pattern of SOA$_{rBC}$/rBC was almost

605   opposite to that of rBC. This result likely indicates that most POA$_{rBC}$ species were co-

606   emitted and coated on rBC cores originally, therefore the coating process during rBCc

607   lifecycle was mainly relevant with SOA species rather than POA species. This process

608   is mainly through photochemical reactions, including in-situ oxidation of originally

609   coated POA species (for example, oxidation of HOA-rich plus WS-HOA to LO-

610   OOA$_{rBC}$, then to MO-OOA$_{rBC}$), and partitioning of secondary species formed in gas-

611   phase reactions onto rBC surface. In addition, sulfate and nitrate were both secondarily

612   formed, but sulfate was dominated by photochemical production while nitrate was

613   governed by nocturnal heterogenous formation (as discussed in Section 3.3.2); different

614   diurnal patterns of them (Fig. S9) point to different coating processes too.

615   In this regard, we hereby propose a concept of average coating time (ACT), which

616   is used to roughly estimate the timescales required for secondary components coated

617   onto rBC. The specific method is listed as follows:

618   1. Move forward the diurnal variation of SA$_{rBC}$/rBC (SA represents a secondary

619   aerosol species) for n hours to get a new SA_{rBC}/rBC diurnal pattern, labelled as

620   "$SA_{rBC}/rBC(r$-nh-ahead)". Here, the r value is the linear correlation coefficient between

621   the new SA_{rBC}/rBC diurnal pattern with that of rBC.

622   2. Choose the best correlation coefficient (r-nh-ahead), and nh corresponds to the

623   ACT for this secondary component.

624   It should be noted that the diurnal pattern of rBC might be affected by the changes

625   of plantenary boundary layer (PBL) height, so that low PBL height could lead to high

626   rBC concentrations during nighttime. We thus used SA_{rBC}/rBC rather than SA_{rBC} here

627   to perform the correlation analyses with rBC. The relative variability of secondary

628   species to rBC might be a good way to eliminate the impacts of PBL, and better

629   represent the "coating process". Nevertheless, one should be cautious that this treatment

630   is only a rough approximation of the "coating process". Diurnal patterns of LO-

631   OOA_{rBC}/rBC and MO-OOA_{rBC}/rBC are depicted in Fig. 10b. They were both opposite

632   to the trend of rBC, and they were similar to each other, except that MO-OOA_{rBC}/rBC

633   peaked hours later in the afternoon, signifying that the MO-OOA_{rBC} needs longer time

634   to coated on rBC than LO-OOA_{rBC} does, consistent with the fact that MO-OOA_{rBC} was

635   "more aged". Correspondingly, we obtained an ACT of 7 hours for MO-OOA_{rBC} (*0.35-*

636   *7*h-ahead) and 5 hours for LO-OOA_{rBC} (*0.57-5*h-ahead) (Fig. 10c) using the method

637   described above. The ACT of sulfate (*0.65-7*h-ahead) and nitrate (*0.30-19*h-ahead) were

638   7 and 19 hours, respectively (Fig. 10d). The results suggest that the rBC emitted mainly

639   in the morning rush hours requires a few hours to be adequately coated by LO-OOA_{rBC},

640   MO-OOA_{rBC} and sulfate, as these three species are mainly produced in the afternoon

641   by photochemical reactions; while photochemical production of nitrate is insignificant,

642   thus rBC was coated by nitrate until later night when nitrate was formed efficiently by

643   heterogenous N_2O_5 hydrolysis. Note the best r values were not high (for example, 0.35

644   for MO-OOA_{rBC} and 0.30 for nitrate), yet the adjusted trends of all secondary

645   components (Figs. 10c and 10d) matched that of rBC quite well during 3:00~12:00 (r

646   of 0.90, 0.91, 0.84 and 0.84 for MO-OOA_{rBC}, LO-OOA_{rBC}, sulfate and nitrate,

647   respectively), likely meaning that daytime variations of two SOAs and sulfate were

648   indeed controlled by the coating process while governing factors of their nighttime

649   variations might be complex, and *vice versa* for nitrate.

650

651   **3.4 Size-resolved hygroscopicity of *r*BCc**

652   By using the method in Section 2.3, we calculated the size-resolved hygroscopicity

653   parameters for the total *r*BCc ($\kappa_{r\text{BCc}}$) and the coatings materials (κ_{CT}) across the whole

654   campaign. The image plots are illustrated in Figs. 11a and 11b. Generally, large $\kappa_{r\text{BCc}}$

655   and κ_{CT} values occurred at big particle sizes, and this result was overall similar to that

656   in Nanjing during winter (Wu et al., 2019). We further illustrate the size-resolved $\kappa_{r\text{BCc}}$

657   as a function of R_{BC} in Fig. 11c. The figure shows that $\kappa_{r\text{BCc}}$ overall became larger with

658   increasing particle size regardless of the coating thickness. However, there were some

659   (though not significant) relatively high $\kappa_{r\text{BCc}}$ values in the range of 80-150 nm (bottom

660   left and bottom right in Fig. 11c).

661   In Figs. 12a and 12b, we further determined the average size-resolved $\kappa_{r\text{BCc}}$ and

662   κ_{CT} as a function of coated diameter ($D_{r\text{BCc}}$). Both $\kappa_{r\text{BCc}}$ and κ_{CT} values were relatively

663   high at $D_{r\text{BCc}}$<100 nm and presented slight decreases from 100 to 150 nm. This is

664   distinctive from those observed in Nanjing, where κ_{CT} increased with $D_{r\text{BCc}}$ from 50 nm

665   (Wu et al., 2019). From Figs. 4b and 4d, it can be seen the *r*BCc with $D_{r\text{BCc}}$<150 nm

666   was dominated by a portion of ammonium and sulfate (8-10%) and organics (~60%),

667   of which organics was dominated by WS-HOA. Such composition explains the

668   relatively high hygroscopicity at $D_{r\text{BCc}}$<150 nm as both ammonium sulfate and WS-

669   HOA are hydrophilic; a slight decrease of the hygroscopicity from 100 to 150 nm $D_{r\text{BCc}}$

670   was also a response of decreased mass contributions of ammonium sulfate and WS-

671   HOA (and increase of hydrophobic HOA-rich contribution).

672   Figures 12a and 12b also provide the fitted exponential functions for the mean

673     $\kappa_{r\text{BCc}}$ and κ_{CT} with $D_{r\text{BCc}}$. The equations are: $\kappa_{r\text{BCc}}(x)= 0.29-0.14 \times \exp(-0.006 \times x)$ and

674     $\kappa_{\text{CT}}(x) = 0.35 - 0.09 \times \exp(-0.003 \times x)$ (x is $D_{r\text{BCc}}$, 150<x<1000 nm). Here, 0.29 and

675   0.35 are the upper limits of $\kappa_{r\text{BCc}}$ and κ_{CT}, higher than those reported in Nanjing (0.28

676   and 0.30 for $\kappa_{r\text{BCc}}$ and κ_{CT}); yet the increasing rates of $\kappa_{r\text{BCc}}$ and κ_{CT} with $D_{r\text{BCc}}$ are 0.14

677   and 0.09, respectively, which are much lower than those from Nanjing (0.35 and 0.27

678   for $\kappa_{r\text{BCc}}$ and κ_{CT})(Wu et al., 2019). Smaller increased contributions of hydrophilic

679 secondary species from 150 to 1000 nm in Shanghai than those from 100 to 1000 nm

680 in Nanjing are likely the cause of smaller increasing rates of hygroscopicity parameters.

681 In addition, it should be noted that the hygroscopicity is not only determined by the

682 bulk composition, but also affected by the phase state of particles. For instance, a recent

683 study reveals that the hygroscopic growth of phase-separated particles (with ammonium

684 sulfate as cores) can be reduced by the secondary organic shells and is dependent on

685 the thickness of organic coating (Li et al., 2021).

686  The critical supersaturation (SS_C) for a selected dry diameter (D_{rBCc} measured by

687 SP-AMS) of a rBCc particle with a hygroscopicity parameter κ_{rBCc}, can be calculated

688 by the "κ-Kohler theory" equation (Petters and Kreidenweis, 2007). Based on the size-

689 resolved κ_{rBCc}, the CCN activation diameter (D_{50}) of particles at a given critical SS_C can

690 be calculated (Wu et al., 2019). Then, by combining the measured rBCc number size

691 distribution and the D_{50} value, activation fraction (f_{AC}) of rBCc number population (i.e.,

692 the fraction greater than the D_{50}) can be obtained. Figure 12c shows the SS_C as a

693 function of D_{rBCc} for the entire sampling period to obtain the D_{50} at a specific SS_C. The

694 D_{50} values of the rBCc particles were determined to be 166 ($\pm$ 16) nm and 110 ($\pm$ 5) nm

695 for SS_C of 0.1% and 0.2%, respectively. The two D_{50} values are both smaller than those

696 determined for rBCc particle in Nanjing (Wu et al., 2019), likely owing to the presence

697 of WS-HOA in Shanghai. Figure 12d shows the f_{AC} at SS_C of 0.1% (D_{50} of 166 nm) was

698 16 ($\pm$ 3)%, and the f_{AC} at SS_C of 0.2% (D_{50} of 110 nm) was 59 ($\pm$ 4)%.

699

700 **3.5 A case study influenced by ship emissions**

701 **3.5.1 Potential source areas of rBCc**

702  To explore the potential geographic origins of rBCc at the receptor site, the hybrid

703 single-particle Lagrangian integrated trajectory (HYSPLIT) model (version 4.9) was

704 applied here. The backward trajectories were classified into four air mass clusters (Fig.

705 S12a), including one long-range transport from northern sea (Cluster1), one long-range

706 transport from northeastern sea (Cluster2), a local one from eastern ports (Cluster3),

707 and one from northwestern inland region (Cluster4). The four clusters occupied 23.8%,

708 33.8%, 37.3%, and 5.0% of the total trajectories, respectively. It is clear that the

709 sampling period was influenced by offshore air masses in most of the time (95%).

710 Cluster3 had the highest mean rBCc concentrations (13.2 ± 10.9 μg m^{-3}) while the mean

711 concentrations of the other three clusters were apparently lower (4.3~5.2 μg m^{-3}). This

712 result is plausible as Cluster3 was the shortest in length therefore was least diluted

713 compared with other three clusters. Average chemical compositions of the rBCc from

714 four clusters (Fig. S12b) showed some differences as well: Cluster1 and Cluster2 had

715 higher MO-OOA$_{rBC}$ contributions, possibly owing to the interceptions of more aged

716 SOA species during the long-range transports; While Cluster4 had less MO-OOA$_{rBC}$

717 but a bit more POA$_{rBC}$ contributions, likely attributing to more primary species emitted

718 in inland regions (similarly, a higher fraction of nitrate was likely because of enhanced

719 NO$_2$ emissions).

720

721 **3.5.2 A typical case of rBCc affected by ship emissions**

722 Ship emissions are found to have an important impact on the air quality of

723 Shanghai and the Yangtze River Delta (Zhao et al., 2013;Fan et al., 2016;Liu et al.,

724 2017b;Chen et al., 2019). The ship engines usually burn heavy fuel oil (HFO), and

725 vanadium (V) and nickel (Ni) can be adopted as reliable tracers for the ship-emitted

726 particles (Ault et al., 2009;Moldanová et al., 2009;Ault et al., 2010). The long-term

727 variation of Ni/V ratio in ship-emitted particles in Shanghai has been recently reported

728 (Yu et al., 2021). The main conclusion is that Ni/V ratio was close to 0.4 in 2018, while

729 it became to be greater than 2.0 in 2020. Our measurement was carried out in 2018, and

730 we therefore chose a period from November 3rd to 5th as a typical case affected by ship

731 emissions (SEP period), since the average Ni/V ratio was ~0.50 and high concentrations

732 of both Ni and V were found. Figure S13 shows the concentration-weighted trajectories

733 (CWT) of ship emission tracers (V, Ni), rBC and rBC-rich factor during SEP, displaying

734 that these components were mainly from sea. During SEP, the correlation coefficient (r)

735 between V(Ni) and rBC was 0.69 (0.74), indicating the SEP was indeed impacted by

736 ship emissions.

737 Figure 13 displays the chemical characteristics of rBCc and NR-PM$_1$ components

738 (especially the OA factors), V and Ni, gaseous pollutants and the meteorological

739 parameters during SEP. As a comparison, we also selected a period with no ship

740 emissions with the same time span as SEP (from 0:00 on November 10 to 0:00 on

741 November 12, termed as non-SEP), and a similar plot during non-SEP is presented in

742 Fig. S14. During SEP, the wind was mainly from east, and the average wind speed was

743 ~0.5 ($\pm$ 0.3) m s^{-1}; Wusong, Luojing and Waigaoqiao ports located northeast of the

744 sampling site (Fig. S1). Instead, the wind was mainly from north during non-SEP.

745 During SEP, the average mass concentrations of V and Ni were 6.3 ($\pm$ 3.1) ng m^{-3} and

746 3.2 ($\pm$ 1.4) ng m^{-3}, respectively, while those during non-SEP were only 2.9 ($\pm$ 1.4) ng

747 m^{-3} and 2.6 ($\pm$ 1.6) ng m^{-3}. The average mass ratio of V/Ni during SEP was 2.0 in

748 agreement with those reported in ship-influenced PM$_1$ (Mazzei et al., 2008;Mar et al.,

749 2009), and within the range of 1.9 to 3.5 for domestic HFO (Zhao et al., 2013), while

750 the average ratio of V/Ni (1.1$\pm$ 0.8) during non-SEP was outside the range. Moreover,

751 the major air pollutants emitted from ships include nitrogen oxides (NO$_x$), sulfur oxides

752 (SO$_2$), carbon monoxide (CO), hydrocarbons and primary/secondary particles (Becagli

753 et al., 2017;Wu et al., 2021). As demonstrated in Fig. 13b and Fig. S14b, SO$_2$

754 concentration was overall higher during SEP (10:00-16:00 on November 11 not

755 included); mass loading of NO$_2$ was higher during the rush hours of non-SEP, but was

756 higher at night (no traffic) during SEP. Mass proportion of sulfate in NR-PM$_1$ during

757 SEP was also higher than that during non-SEP (22.7 $\pm$ 8.1 % *vs.* 19.1$\pm$ 5.3 %), but *vice*

758 *versa* for nitrate (17.8 ($\pm$ 9.9)% during SEP *vs.* 26.2 ($\pm$ 9.1)% during non-SEP).

759 We further investigated the dependences of *r*BCc and NR-PM$_1$ species on V during

760 SEP and non-SEP, as shown in Fig. S15. Here we only used V since Ni level might be

761 influenced by other emission sources, such as refining industry (Jang et al., 2007;Kim

762 et al., 2014) in urban Shanghai, and during non-SEP, Ni still presented a good

763 correlation with *r*BC (*r*=0.80). During SEP, V concentrations (most of them >4 ng m^{-3})

764 overall positively correlated with both sulfate and nitrate (except for *r*BCc sulfate) (Fig.

765 S15a). Considering that V concentration was independently measured for all fine

766 particles, a better correlation with total NR-PM$_1$ sulfate than it with *r*BCc sulfate is

767 reasonable. Similarly, V-rich particles had positive correlations with traffic-related OA

768 and LO-OOA no matter in *r*BCc or in total NR-PM$_1$ (Fig. S15b). Conversely, during

769   non-SEP, particles with low-V content (most of them <4 ng m^{-3}) had no clear links with

770   sulfate, nitrate, POA and SOA species (even anti-correlations for V>2.5 ng m^{-3}) (Figs.

771   S15c and S15d; a detailed comparison of the correlation coefficients of V with OA

772   factors of rBCc and NR-PM$_1$ organics are provided in Table S2). The results above

773   demonstrate that during SEP, chemical properties of the particles (both fresh and aged

774   ones) were clearly linked with ship influences.

775   Previous studies (Ault et al., 2009;Ault et al., 2010;Liu et al., 2017b) have shown

776   that the fresh ship-emitted V-rich particles are typically accompanied by high sulfate

777   contribution, while those aged V-containing ship particles are on the other hand with

778   relatively high nitrate contribution. In order to further probe chemical characteristics

779   and evolution processes of particles influenced by ship emissions, we divided SEP into

780   three episodes (i.e., EP1-EP3) (marked in Fig. 13). During EP1, rBC content was

781   highest (Fig. 13i) and coating was thinnest (Fig. S16i) indicating the particles were

782   relatively fresh, nevertheless the SOA contents were not low (Figs.13h and 13j), OS$_C$

783   was moderate (Fig. S16j), sulfate portions in NR-PM$_1$ and rBCc were both the highest

784   (26.5%), and nitrate portion was the lowest (9.8%) among three episodes (Figs.13g and

785   13i). Such composition is not common in other cases, demonstrating it was a specific

786   period impacted by fresh ship emissions. EP2 had the highest mass loadings of V, gas

787   pollutants as well as the lowest PBL height (~200 meters) (Fig. S16). Mass

788   contributions of nitrate increased and sulfate decreased, and rBC content decreased

789   from those during EP1, signifying that the particle population likely contained some

790   aged ship-emitted particles. Surely, particle composition during EP2 was also

791   influenced by the formation mechanisms of secondary species: EP2 was mostly during

792   nighttime, therefore photochemical formation of sulfate and SOA were weak (as shown

793   in Figs. 13g and 13j, sulfate contribution was only 15.1%, and SOA contribution was

794   only 33.7%), while nitrate formation was enhanced due to the nocturnal process. During

795   EP3, rBC was the lowest, sulfate and V were moderate, nitrate and SOA were highest

796   in both rBCc and NR-PM$_1$, OS$_C$ and R_{BC} were highest in rBCc among the three episodes

797   (Figs. 13i-j and Figs. S16i-k), therefore it was also a period with influence from aged

798   ship-emitted particles; the difference from EP2 is that photochemically formed sulfate

799   and SOA were still significant as EP3 was in the later afternoon and early evening,

800   though heterogeneously formed nitrate played a non-negligible role too (see the

801   increase of RH, increase of nitrate and decrease of O_3 concentrations from the

802   beginning of EP3 in Fig. 13).

803

804   **4. Conclusions and implications**

805   We conducted a field measurement during November of 2018 in urban Shanghai,

806   China, focusing on the elucidation of physical and chemical properties of the ambient

807   particles containing rBC cores (rBCc) by using a laser-only SP-AMS together with a

808   HR-AMS. The campaign-average rBCc was 4.6 ($\pm$ 4.4) μg m^{-3}, occupying ~19.1 ($\pm$

809   4.9) % mass of the total NR-PM$_1$. The average mass ratio of coating to rBC cores (R_{BC})

810   was ~5.0 ($\pm$ 1.7), indicating an overall thick coating, compared with the rBCc near

811   combustion source. Sulfate was found to preferentially condense on non-rBC particles

812   thus led to a low fraction of rBCc sulfate to that in NR-PM$_1$ (7.4% $\pm$ 2.2 %), while

813   distribution of nitrate between rBCc and non-rBC particles showed no obvious

814   difference. PMF analysis on rBCc and NR-PM$_1$ OA reveals that cooking-related

815   organics were externally mixed with rBC, and a small portion of organics from biomass

816   burning was only present in rBCc; the traffic-related OA species, however, was in a

817   large part internally mixed with rBC.

818   A regression algorithm was applied to deconvolute the size distributions of

819   individual rBCc OA factors, and results show that small rBCc particles were

820   predominantly generated from traffic, and such particles could grow bigger because of

821   condensation of secondary inorganic and organic components, resulting in thick coating.

822   Investigation on diurnal patterns of the rBCc species reveals that sulfate and two SOA

823   factors (LO-OOA$_{rBC}$ and MO-OOA$_{rBC}$) were generated mainly through daytime

824   photochemical oxidation; nitrate, on the other hand, was governed mainly by the

825   nocturnal N_2O_5 hydrolysis. Partial SOA was found to be produced from in-situ

826   photochemical conversion from traffic-related POA. An average coating time (ACT)

827   was proposed to roughly estimate the timescales for the secondary species to coat on

828   rBC, and the ACT of sulfate, LO-OOA$_{rBC}$, MO-OOA$_{rBC}$ and nitrate were approximately

829   7, 5, 7 and 19 hours, respectively.

830   Moreover, the size-resolved hygroscopicity parameters of rBCc particles ($\kappa_{r\text{BCc}}$)

831   and the coating material (κ_{CT}) were obtained based on the elucidated composition of

832   rBCc particles. The fitted equations are: $\kappa_{r\text{BCc}}(x) = 0.29 - 0.14 \times \exp(-0.006 \times x)$ and

833   $\kappa_{\text{CT}}(x) = 0.35 - 0.09 \times \exp(-0.003 \times x)$ (x is $D_{r\text{BCc}}$, $150 < x < 1000$ nm). The minimums

834   of both $\kappa_{r\text{BCc}}$ and κ_{CT} were at ~150 nm due to the abundances of hydrophobic rBC cores

835   and traffic-related HOA at this size. Under critical supersaturations (SS_C) of 0.1% and

836   0.2%, the D_{50} values were estimated to be 166 ($\pm$ 16) and 110 ($\pm$ 5) nm, and the

837   activated number fractions of rBCc particles were 16 ($\pm$ 3)% and 59 ($\pm$ 4)%,

838   respectively. Finally, a typical case with influence from ship emissions was investigated.

839   During this period, the rBCc particles were enriched in V (6.3 $\pm$ 3.1 ng m^{-3}), with a

840   V/Ni ratio of 2.0 ($\pm$ 0.6), and various secondary formation processes affect the ship-

841   emitted particles at different times of the day.

842   In summary, the findings from this comprehensive study on rBCc provide rich

843   information regarding the various primary sources and secondary formation pathways

844   of species coated on rBC, as well as the features of distributions of those species

845   between rBC and non-rBC particles. In particular, different types of rBCc particles

846   from diesel and gasoline vehicle emissions were resolved and elucidation of their

847   properties are useful to their future effective control. Understanding of the formation

848   processes and coating timescales of secondary components is helpful to understand the

849   impact of ambient BC particles too. At last, the parameterized relationship of

850   hygroscopicity with size distribution is useful for modelling the climate effect of rBC

851   (alternation of cloud properties).

852

853   *Data availability.* The data in this study are available from the authors upon request

854   (caxinra@163.com).

855

856   *Supplement.* The supplement related to this article is available online at: XXX

857

858   *Author contributions.* SJC, DDH, YZW, JFW, FZS, and XLG conducted the field

859 measurement. SJC, DDH, YZW, JFW, and JKX analyzed the data. YJZ, HLW, CH and
860 HL reviewed the paper and provide useful suggestions. SJC and XLG wrote the paper.
861

862 *Competing interests.* The contact author has declared that neither they nor their co-
863 authors have any competing interests.
864

865 *Disclaimer.* Publisher's note: Copernicus Publications remains neutral with regard to
866 jurisdictional claims in published maps and institutional affiliations.
867

868 *Acknowledgements.* We sincerely thank SAES to provide data of gaseous pollutants and
869 particulate V and Ni, and the logistic help during the campaign.
870

871 *Financial support.* This work has been supported by the National Natural Science
872 Foundation of China (42021004, 21976093 and 21777073).
873

874 *Review statement*. This paper was XXX.
875

876 **References**

877 Aiken, A. C., DeCarlo, P. F., Kroll, J. H., Worsnop, D. R., Huffman, J. A., Docherty,
878 K. S., Ulbrich, I. M., Mohr, C., Kimmel, J. R., Sueper, D., Sun, Y., Zhang, Q., Trimborn,
879 A., Northway, M., Ziemann, P. J., Canagaratna, M. R., Onasch, T. B., Alfarra, M. R.,
880 Prevot, A. S. H., Dommen, J., Duplissy, J., Metzger, A., Baltensperger, U., and Jimenez,
881 J. L.: O/C and OM/OC ratios of primary, secondary, and ambient organic aerosols with
882 high-resolution time-of-flight aerosol mass spectrometry, Environ. Sci. Technol., 42,
883 4478-4485, https://doi.org/10.1021/es703009q, 2008.

884 Ault, A. P., Moore, M. J., Furutani, H., and Prather, K. A.: Impact of emissions
885 from the Los Angeles port region on San Diego air quality during regional transport
886 events, Environ. Sci. Technol., 43, 3500-3506, https://doi.org/10.1021/es8018918,
887 2009.

888 Ault, A. P., Gaston, C. I., Ying, W., Gerardo, D., Thiemens, M. H., and Prather, K.

889 A.: Characterization of the single particle mixing state of individual ship plume events

890 measured at the Port of Los Angeles, Environ. Sci. Technol., 44, 1954-1961,

891 https://doi.org/10.1021/es902985h, 2010.

892 Becagli, S., Anello, F., Bommarito, C., Cassola, F., Calzolai, G., Di Iorio, T., di

893 Sarra, A., Gómez-Amo, J.-L., Lucarelli, F., Marconi, M., Meloni, D., Monteleone, F.,

894 Nava, S., Pace, G., Severi, M., Sferlazzo, D. M., Traversi, R., and Udisti, R.:

895 Constraining the ship contribution to the aerosol of the central Mediterranean, Atmos.

896 Chem. Phys., 17, 2067-2084, https://doi.org/10.5194/acp-17-2067-2017, 2017.

897 Bond, T. C., Doherty, S. J., Fahey, D. W., Forster, P. M., Berntsen, T., DeAngelo,

898 B. J., Flanner, M. G., Ghan, S., Kärcher, B., Koch, D., Kinne, S., Kondo, Y., Quinn, P.

899 K., Sarofim, M. C., Schultz, M. G., Schulz, M., Venkataraman, C., Zhang, H., Zhang,

900 S., Bellouin, N., Guttikunda, S. K., Hopke, P. K., Jacobson, M. Z., Kaiser, J. W.,

901 Klimont, Z., Lohmann, U., Schwarz, J. P., Shindell, D., Storelvmo, T., Warren, S. G.,

902 and Zender, C. S.: Bounding the role of black carbon in the climate system: A scientific

903 assessment, J. Geophys. Res.: Atmos., 118, 5380-5552,

904 https://doi.org/10.1002/jgrd.50171, 2013.

905 Canagaratna, M. R., Jayne, J. T., Jimenez, J. L., Allan, J. D., Alfarra, M. R., Zhang,

906 Q., Onasch, T. B., Drewnick, F., Coe, H., Middlebrook, A., Delia, A., Williams, L. R.,

907 Trimborn, A. M., Northway, M. J., DeCarlo, P. F., Kolb, C. E., Davidovits, P., and

908 Worsnop, D. R.: Chemical and microphysical characterization of ambient aerosols with

909 the aerodyne aerosol mass spectrometer, Mass Spectrom. Rev., 26, 185-222,

910 https://doi.org/10.1002/mas.20115, 2007.

911 Canagaratna, M. R., Jimenez, J. L., Kroll, J. H., Chen, Q., Kessler, S. H., Massoli,

912 P., Hildebrandt Ruiz, L., Fortner, E., Williams, L. R., Wilson, K. R., Surratt, J. D.,

913 Donahue, N. M., Jayne, J. T., and Worsnop, D. R.: Elemental ratio measurements of

914 organic compounds using aerosol mass spectrometry: characterization, improved

915 calibration, and implications, Atmos. Chem. Phys., 15, 253-272,

916 https://doi.org/10.5194/acp-15-253-2015, 2015a.

917 Canagaratna, M. R., Massoli, P., Browne, E. C., Franklin, J. P., Wilson, K. R.,

918 Onasch, T. B., Kirchstetter, T. W., Fortner, E. C., Kolb, C. E., Jayne, J. T., Kroll, J. H.,

919   and Worsnop, D. R.: Chemical compositions of black carbon particle cores and coatings

920   via soot particle aerosol mass spectrometry with photoionization and electron ionization,

921   J. Phys. Chem. A, 119, 4589-4599, https://doi.org/10.1021/jp510711u, 2015b.

922   Cao, L.-M., Wei, J., He, L.-Y., Zeng, H., Li, M.-L., Zhu, Q., Yu, G.-H., and Huang,

923   X.-F.: Aqueous aging of secondary organic aerosol coating onto black carbon: Insights

924   from simultaneous L-ToF-AMS and SP-AMS measurements at an urban site in

925   southern   China,   J.   Clean   Prod.,   330,   129888,

926   https://doi.org/10.1016/j.jclepro.2021.129888, 2022.

927   Cappa, C. D., Onasch, T. B., Massoli, P., Worsnop, D. R., Bates, T. S., Cross, E.

928   S., Davidovits, P., Hakala, J., Hayden, K. L., Jobson, B. T., Kolesar, K. R., Lack, D. A.,

929   Lerner, B. M., Li, S.-M., Mellon, D., Nuaaman, I., Olfert, J. S., Petäjä, T., Quinn, P. K.,

930   Song, C., Subramanian, R., Williams, E. J., and Zaveri, R. A.: Radiative Absorption

931   Enhancements Due to the Mixing State of Atmospheric Black Carbon, Science, 337,

932   1078-1081, https://doi.org/10.1126/science.1230260, 2012.

933   Chang, R. Y. W., Slowik, J. G., Shantz, N. C., Vlasenko, A., Liggio, J., Sjostedt, S.

934   J., Leaitch, W. R., and Abbatt, J. P. D.: The hygroscopicity parameter (κ) of ambient

935   organic aerosol at a field site subject to biogenic and anthropogenic influences:

936   relationship to degree of aerosol oxidation, Atmos. Chem. Phys., 10, 5047-5064,

937   https://doi.org/10.5194/acp-10-5047-2010, 2010.

938   Chen, B., Bai, Z., Cui, X., Chen, J., Andersson, A., and Gustafsson, O.: Light

939   absorption enhancement of black carbon from urban haze in Northern China winter,

940   Environ. Pollut., 221, 418-426, https://doi.org/10.1016/j.envpol.2016.12.004, 2017.

941   Chen, C., Fan, X., Shaltout, T., Qiu, C., Ma, Y., Goldman, A., and Khalizov, A. F.:

942   An unexpected restructuring of combustion soot aggregates by subnanometer coatings

943   of polycyclic aromatic hydrocarbons, Geophys. Res. Lett., 43, 11,080-011,088,

944   https://doi.org/10.1002/2016GL070877, 2016.

945   Chen, C., Enekwizu, O. Y., Fan, X., Dobrzanski, C. D., Ivanova, E. V., Ma, Y., Gor,

946   G. Y., and Khalizov, A. F.: Single Parameter for Predicting the Morphology of

947   Atmospheric   Black   Carbon,   Environ.   Sci.   Technol.,   52,   14169-14179,

948   https://doi.org/10.1021/acs.est.8b04201, 2018.

Chen, D., Tian, X., Lang, J., Zhou, Y., Li, Y., Guo, X., Wang, W., and Liu, B.: The impact of ship emissions on PM2.5 and the deposition of nitrogen and sulfur in Yangtze River Delta, China, Sci. Total Environ., 649, 1609-1619, https://doi.org/10.1016/j.scitotenv.2018.08.313, 2019.

Clegg, S. L., Brimblecombe, P., and Wexler, A. S.: Thermodynamic model of the system H+− NH4+− SO42-− NO3-− H2O at tropospheric temperatures, 102, 2155–2171, https://doi.org/10.1021/jp973043j, 1998.

Collier, S., Williams, L. R., Onasch, T. B., Cappa, C. D., Zhang, X., Russell, L. M., Chen, C.-L., Sanchez, K. J., Worsnop, D. R., and Zhang, Q.: Influence of Emissions and Aqueous Processing on Particles Containing Black Carbon in a Polluted Urban Environment: Insights From a Soot Particle-Aerosol Mass Spectrometer, J. Geophys. Res.: Atmos., 123, 6648-6666, https://doi.org/10.1002/2017jd027851, 2018.

Corbin, J. C., Sierau, B., Gysel, M., Laborde, M., Keller, A., Kim, J., Petzold, A., Onasch, T. B., Lohmann, U., and Mensah, A. A.: Mass spectrometry of refractory black carbon particles from six sources: carbon-cluster and oxygenated ions, Atmos. Chem. Phys., 14, 2591-2603, https://doi.org/10.5194/acp-14-2591-2014, 2014.

Cubison, M. J., Ortega, A. M., Hayes, P. L., Farmer, D. K., Day, D., Lechner, M. J., Brune, W. H., Apel, E., Diskin, G. S., Fisher, J. A., Fuelberg, H. E., Hecobian, A., Knapp, D. J., Mikoviny, T., Riemer, D., Sachse, G. W., Sessions, W., Weber, R. J., Weinheimer, A. J., Wisthaler, A., and Jimenez, J. L.: Effects of aging on organic aerosol from open biomass burning smoke in aircraft and laboratory studies, Atmos. Chem. Phys., 11, 12049-12064, https://doi.org/10.5194/acp-11-12049-2011, 2011.

DeCarlo, P. F., Kimmel, J. R., Trimborn, A., Northway, M. J., Jayne, J. T., Aiken, A. C., Gonin, M., Fuhrer, K., Horvath, T., Docherty, K. S., Worsnop, D. R., and Jimenez, J. L.: Field-Deployable, High-Resolution, Time-of-Flight Aerosol Mass Spectrometer, Anal. Chem. , 78, 8281-8289, https://doi.org/10.1021/ac061249n, 2006.

Enroth, J., Saarikoski, S., Niemi, J., Kousa, A., Ježek, I., Močnik, G., Carbone, S., Kuuluvainen, H., Rönkkö, T., Hillamo, R., and Pirjola, L.: Chemical and physical characterization of traffic particles in four different highway environments in the Helsinki metropolitan area, Atmos. Chem. Phys., 16, 5497-5512,

https://doi.org/10.5194/acp-16-5497-2016, 2016.

Fan, Q., Zhang, Y., Ma, W., Ma, H., Feng, J., Yu, Q., Yang, X., Ng, S. K., Fu, Q., and Chen, L.: Spatial and Seasonal Dynamics of Ship Emissions over the Yangtze River Delta and East China Sea and Their Potential Environmental Influence, Environ. Sci. Technol., 50, 1322-1329, https://doi.org/10.1021/acs.est.5b03965, 2016.

Gao, X., Yang, L., Cheng, S., Gao, R., Zhou, Y., Xue, L., Shou, Y., Wang, J., Wang, X., Nie, W., Xu, P., and Wang, W.: Semi-continuous measurement of water-soluble ions in PM2.5 in Jinan, China: Temporal variations and source apportionments, Atmos. Environ., 45, 6048-6056, https://doi.org/10.1016/j.atmosenv.2011.07.041, 2011.

Ge, X., Zhang, Q., Sun, Y., Ruehl, C. R., and Setyan, A.: Effect of aqueous-phase processing on aerosol chemistry and size distributions in Fresno, California, during wintertime, Environ. Chem., 9, 221-235, https://doi.org/10.1071/EN11168, 2012.

Gilardoni, S., Massoli, P., Paglione, M., Giulianelli, L., Carbone, C., Rinaldi, M., Decesari, S., Sandrini, S., Costabile, F., Gobbi, G. P., Pietrogrande, M. C., Visentin, M., Scotto, F., Fuzzi, S., and Facchini, M. C.: Direct observation of aqueous secondary organic aerosol from biomass-burning emissions, Proc. Natl. Acad. Sci. U. S. A., 113, 10013-10018, https://doi.org/10.1073/pnas.1602212113, 2016.

Gong, X., Zhang, C., Chen, H., Nizkorodov, S. A., Chen, J., and Yang, X.: Size distribution and mixing state of black carbon particles during a heavy air pollution episode in Shanghai, Atmos. Chem. Phys., 16, 5399-5411, https://doi.org/10.5194/acp-16-5399-2016, 2016.

Gysel, M., Crosier, J., Topping, D. O., Whitehead, J. D., Bower, K. N., Cubison, M. J., Williams, P. I., Flynn, M. J., McFiggans, G. B., and Coe, H.: Closure study between chemical composition and hygroscopic growth of aerosol particles during TORCH2, Atmos. Chem. Phys., 7, 6131-6144, https://doi.org/10.5194/acp-7-6131-2007, 2007.

Heald, C. L., Kroll, J. H., Jimenez, J. L., Docherty, K. S., DeCarlo, P. F., Aiken, A. C., Chen, Q., Martin, S. T., Farmer, D. K., and Artaxo, P.: A simplified description of the evolution of organic aerosol composition in the atmosphere, Geophys. Res. Lett., 37, https://doi.org/10.1029/2010gl042737, 2010.

1009   Hu, D., Liu, D., Kong, S., Zhao, D., Wu, Y., Li, S., Ding, S., Zheng, S., Cheng, Y.,

1010   Hu, K., Deng, Z., Wu, Y., Tian, P., Liu, Q., Huang, M., and Ding, D.: Direct

1011   Quantification of Droplet Activation of Ambient Black Carbon Under Water

1012   Supersaturation, J. Geophys. Res.: Atmos., 126, e2021JD034649,

1013   https://doi.org/10.1029/2021jd034649, 2021.

1014   Jacobi, H. W., Lim, S., Ménégoz, M., Ginot, P., Laj, P., Bonasoni, P., Stocchi, P.,

1015   Marinoni, A., and Arnaud, Y.: Black carbon in snow in the upper Himalayan Khumbu

1016   Valley, Nepal: observations and modeling of the impact on snow albedo, melting, and

1017   radiative forcing, The Cryosphere, 9, 1685-1699, https://doi.org/10.5194/tc-9-1685-

1018   2015, 2015.

1019   Jang, H.-N., Seo, Y.-C., Lee, J.-H., Hwang, K.-W., Yoo, J.-I., Sok, C.-H., and Kim,

1020   S.-H.: Formation of fine particles enriched by V and Ni from heavy oil combustion:

1021   Anthropogenic sources and drop-tube furnace experiments, Atmos. Environ., 41, 1053-

1022   1063, https://doi.org/10.1016/j.atmosenv.2006.09.011, 2007.

1023   Jayne, J. T., Leard, D. C., Zhang, X., Davidovits, P., Smith, K. A., Kolb, C. E., and

1024   Worsnop, D. R.: Development of an aerosol mass spectrometer for size and composition

1025   analysis of submicron particles, Aerosol Sci. Technol., 33, 49-70,

1026   https://doi.org/10.1080/027868200410840, 2000.

1027   Kim, K.-H., Shon, Z.-H., Mauulida, P. T., and Song, S.-K.: Long-term monitoring

1028   of airborne nickel (Ni) pollution in association with some potential source processes in

1029   the urban environment, Chemosphere, 111, 312-319,

1030   https://doi.org/10.1016/j.chemosphere.2014.03.138, 2014.

1031   Kroll, J. H., Donahue, N. M., Jimenez, J. L., Kessler, S. H., Canagaratna, M. R.,

1032   Wilson, K. R., Altieri, K. E., Mazzoleni, L. R., Wozniak, A. S., Bluhm, H., Mysak, E.

1033   R., Smith, J. D., Kolb, C. E., and Worsnop, D. R.: Carbon oxidation state as a metric

1034   for describing the chemistry of atmospheric organic aerosol, Nat. Chem., 3, 133-139,

1035   https://doi.org/10.1038/nchem.948, 2011.

1036   Lambe, A. T., Ahern, A. T., Wright, J. P., Croasdale, D. R., Davidovits, P., and

1037   Onasch, T. B.: Oxidative aging and cloud condensation nuclei activation of laboratory

1038   combustion soot, J. Aerosol. Sci., 79, 31-39,

1039   https://doi.org/10.1016/j.jaerosci.2014.10.001, 2015.

1040   Laskin, A., Smith, J. S., and Laskin, J.: Molecular characterization of nitrogen-

1041 containing organic compounds in biomass burning aerosols using high-resolution mass

1042 spectrometry, Environ. Sci. Technol., 43, 3764-3771,

1043 https://doi.org/10.1021/es803456n, 2009.

1044   Lee, A. K. Y., Willis, M. D., Healy, R. M., Onasch, T. B., and Abbatt, J. P. D.:

1045 Mixing state of carbonaceous aerosol in an urban environment: single particle

1046 characterization using the soot particle aerosol mass spectrometer (SP-AMS), Atmos.

1047 Chem. Phys., 15, 1823-1841, https://doi.org/10.5194/acp-15-1823-2015, 2015.

1048   Lee, A. K. Y., Chen, C.-L., Liu, J., Price, D. J., Betha, R., Russell, L. M., Zhang,

1049 X., and Cappa, C. D.: Formation of secondary organic aerosol coating on black carbon

1050 particles near vehicular emissions, Atmos. Chem. Phys., 17, 15055-15067,

1051 https://doi.org/10.5194/acp-17-15055-2017, 2017.

1052   Lee, A. K. Y., Rivellini, L. H., Chen, C. L., Liu, J., Price, D. J., Betha, R., Russell,

1053 L. M., Zhang, X., and Cappa, C. D.: Influences of primary emission and secondary

1054 coating formation on the particle diversity and mixing state of black carbon particles,

1055 Environ. Sci. Technol., 53, 9429-9438, https://doi.org/10.1021/acs.est.9b03064, 2019.

1056   Li, W., Teng, X., Chen, X., Liu, L., Xu, L., Zhang, J., Wang, Y., Zhang, Y., and Shi,

1057 Z.: Organic coating reduces hygroscopic growth of phase-separated aerosol particles,

1058 Environ. Sci. Technol., 55, 16339–16346, https://doi.org/10.1021/acs.est.1c05901,

1059 2021.

1060   Liu, D., Allan, J., Whitehead, J., Young, D., Flynn, M., Coe, H., McFiggans, G.,

1061 Fleming, Z. L., and Bandy, B.: Ambient black carbon particle hygroscopic properties

1062 controlled by mixing state and composition, Atmos. Chem. Phys., 13, 2015-2029,

1063 https://doi.org/10.5194/acp-13-2015-2013, 2013.

1064   Liu, D., Whitehead, J., Alfarra, M. R., Reyes-Villegas, E., Spracklen, Dominick V.,

1065 Reddington, Carly L., Kong, S., Williams, Paul I., Ting, Y.-C., Haslett, S., Taylor,

1066 Jonathan W., Flynn, Michael J., Morgan, William T., McFiggans, G., Coe, H., and

1067 Allan, James D.: Black-carbon absorption enhancement in the atmosphere determined

1068 by particle mixing state, Nat. Geosci., 10, 184-188, https://doi.org/10.1038/ngeo2901,

1069   2017a.

1070   Liu, D., Joshi, R., Wang, J., Yu, C., Allan, J. D., Coe, H., Flynn, M. J., Xie, C., Lee,

1071   J., Squires, F., Kotthaus, S., Grimmond, S., Ge, X., Sun, Y., and Fu, P.: Contrasting

1072   physical properties of black carbon in urban Beijing between winter and summer,

1073   Atmos. Chem. Phys., 19, 6749-6769, https://doi.org/10.5194/acp-19-6749-2019, 2019.

1074   Liu, S., Aiken, A. C., Gorkowski, K., Dubey, M. K., Cappa, C. D., Williams, L. R.,

1075   Herndon, S. C., Massoli, P., Fortner, E. C., Chhabra, P. S., Brooks, W. A., Onasch, T.

1076   B., Jayne, J. T., Worsnop, D. R., China, S., Sharma, N., Mazzoleni, C., Xu, L., Ng, N.

1077   L., Liu, D., Allan, J. D., Lee, J. D., Fleming, Z. L., Mohr, C., Zotter, P., Szidat, S., and

1078   Prevot, A. S. H.: Enhanced light absorption by mixed source black and brown carbon

1079   particles in UK winter, Nat. Commun., 6, 8435, https://doi.org/10.1038/ncomms9435,

1080   2015.

1081   Liu, Z., Lu, X., Feng, J., Fan, Q., Zhang, Y., and Yang, X.: Influence of Ship

1082   Emissions on Urban Air Quality: A Comprehensive Study Using Highly Time-Resolved

1083   Online Measurements and Numerical Simulation in Shanghai, Environ. Sci. Technol.,

1084   51, 202-211, https://doi.org/10.1021/acs.est.6b03834, 2017b.

1085   Ma, Y., Huang, C., Jabbour, H., Zheng, Z., Wang, Y., Jiang, Y., Zhu, W., Ge, X.,

1086   Collier, S., and Zheng, J.: Mixing state and light absorption enhancement of black

1087   carbon aerosols in summertime Nanjing, China, Atmos. Environ., 222, 117141,

1088   https://doi.org/https://doi.org/10.1016/j.atmosenv.2019.117141, 2020.

1089   Malmborg, V. B., Eriksson, A. C., Shen, M., Nilsson, P., Gallo, Y., Waldheim, B.,

1090   Martinsson, J., Andersson, O., and Pagels, J.: Evolution of In-Cylinder Diesel Engine

1091   Soot and Emission Characteristics Investigated with Online Aerosol Mass Spectrometry,

1092   Environ. Sci. Technol., 51, 1876-1885, https://doi.org/10.1021/acs.est.6b03391, 2017.

1093   Mar, V., Fulvio, A., Andrés, A., Xavier, Q., Teresa, M., Saúl García, D. S., María

1094   Dolores, H., and Rosalía, F. P.: Chemical tracers of particulate emissions from

1095   commercial   shipping,   Environ.   Sci.   Technol.,   43,   7472-7477,

1096   https://doi.org/10.1021/es901558t, 2009.

1097   Massoli, P., Fortner, E. C., Canagaratna, M. R., Williams, L. R., Zhang, Q., Sun,

1098   Y., Schwab, J. J., Trimborn, A., Onasch, T. B., Demerjian, K. L., Kolb, C. E., Worsnop,

D. R., and Jayne, J. T.: Pollution Gradients and Chemical Characterization of Particulate Matter from Vehicular Traffic near Major Roadways: Results from the 2009 Queens College Air Quality Study in NYC, Aerosol Sci. Technol., 46, 1201-1218, https://doi.org/10.1080/02786826.2012.701784, 2012.

Massoli, P., Onasch, T. B., Cappa, C. D., Nuamaan, I., Hakala, J., Hayden, K., Li, S.-M., Sueper, D. T., Bates, T. S., Quinn, P. K., Jayne, J. T., and Worsnop, D. R.: Characterization of black carbon-containing particles from soot particle aerosol mass spectrometer measurements on the R/VAtlantisduring CalNex 2010, J. Geophys. Res.: Atmos., 120, 2575-2593, https://doi.org/10.1002/2014jd022834, 2015.

Mazzei, F., D'Alessandro, A., Lucarelli, F., Nava, S., Prati, P., Valli, G., and Vecchi, R.: Characterization of particulate matter sources in an urban environment, Sci. Total Environ., 401, 81-89, https://doi.org/10.1016/j.scitotenv.2008.03.008, 2008.

Mohr, C., Huffman, J. A., Cubison, M. J., Aiken, A. C., Docherty, K. S., Kimmel, J. R., Ulbrich, I. M., Hannigan, M., and Jimenez, J. L.: Characterization of Primary Organic Aerosol Emissions from Meat Cooking, Trash Burning, and Motor Vehicles with High-Resolution Aerosol Mass Spectrometry and Comparison with Ambient and Chamber Observations, Environ. Sci. Technol., 43, 2443-2449, https://doi.org/10.1021/es8011518, 2009.

Moldanová, J., Fridell, E., Popovicheva, O., Demirdjian, B., Tishkova, V., Faccinetto, A., and Focsa, C.: Characterisation of particulate matter and gaseous emissions from a large ship diesel engine, Atmos. Environ., 43, 2632-2641, https://doi.org/10.1016/j.atmosenv.2009.02.008, 2009.

Ng, N. L., Canagaratna, M. R., Jimenez, J. L., Chhabra, P. S., Seinfeld, J. H., and Worsnop, D. R.: Changes in organic aerosol composition with aging inferred from aerosol mass spectra, Atmos. Chem. Phys., 11, 6465-6474, https://doi.org/10.5194/acp-11-6465-2011, 2011.

Onasch, T. B., Trimborn, A., Fortner, E. C., Jayne, J. T., Kok, G. L., Williams, L. R., Davidovits, P., and Worsnop, D. R.: Soot Particle Aerosol Mass Spectrometer: Development, Validation, and Initial Application, Aerosol Sci. Technol., 46, 804-817, https://doi.org/10.1080/02786826.2012.663948, 2012.

1129   Paatero, P., and Tapper, U.: Positive matrix factorization: A non-negative factor

1130   model with optimal utilization of error estimates of data values, Environmetrics, 5, 111-

1131   126, https://doi.org/10.1002/env.3170050203, 1994.

1132   Pathak, R. K., Wang, T., and Wu, W. S.: Nighttime enhancement of PM2.5 nitrate

1133   in ammonia-poor atmospheric conditions in Beijing and Shanghai: Plausible

1134   contributions of heterogeneous hydrolysis of N2O5 and HNO3 partitioning, Atmos.

1135   Environ., 45, 1183-1191, https://doi.org/10.1016/j.atmosenv.2010.09.003, 2011.

1136   Peng, J., Hu, M., Guo, S., Du, Z., Zheng, J., Shang, D., Levy, Z. M., Zeng, L.,

1137   Shao, M., and Wu, Y. S.: Markedly enhanced absorption and direct radiative forcing of

1138   black carbon under polluted urban environments, Proc. Natl. Acad. Sci. U. S. A., 113,

1139   4266-4271, https://doi.org/10.1073/pnas.1602310113, 2016.

1140   Petit, J. E., Favez, O., Albinet, A., and Canonaco, F.: A user-friendly tool for

1141   comprehensive evaluation of the geographical origins of atmospheric pollution: Wind

1142   and trajectory analyses, 88, 183-187, https://doi.org/10.1016/j.envsoft.2016.11.022,

1143   2017.

1144   Petters, M. D., and Kreidenweis, S. M.: A single parameter representation of

1145   hygroscopic growth and cloud condensation nucleus activity, Atmos. Chem. Phys., 7,

1146   1961-1971, https://doi.org/10.5194/acp-7-1961-2007, 2007.

1147   Ramanathan, V., and Carmichael, G.: Global and regional climate changes due to

1148   black carbon, Nat. Geosci., 1, 221-227, https://doi.org/10.1038/ngeo156, 2008.

1149   Rivellini, L.-H., Adam, M. G., Kasthuriarachchi, N., and Lee, A. K. Y.:

1150   Characterization of carbonaceous aerosols in Singapore: insight from black carbon

1151   fragments and trace metal ions detected by a soot particle aerosol mass spectrometer,

1152   Atmos. Chem. Phys., 20, 5977-5993, https://doi.org/10.5194/acp-20-5977-2020, 2020.

1153   Saarikoski, S., Timonen, H., Carbone, S., Kuuluvainen, H., Niemi, J. V., Kousa,

1154   A., Rönkkö, T., Worsnop, D., Hillamo, R., and Pirjola, L.: Investigating the chemical

1155   species in submicron particles emitted by city buses, Aerosol Sci. Technol., 51, 317-

1156   329, https://doi.org/10.1080/02786826.2016.1261992, 2016.

1157   Sun, Y. L., Zhang, Q., Schwab, J. J., Demerjian, K. L., Chen, W. N., Bae, M. S.,

1158   Hung, H. M., Hogrefe, O., Frank, B., Rattigan, O. V., and Lin, Y. C.: Characterization

of the sources and processes of organic and inorganic aerosols in New York city with a high-resolution time-of-flight aerosol mass apectrometer, Atmos. Chem. Phys., 11, 1581-1602, https://doi.org/10.5194/acp-11-1581-2011, 2011.

Sun, Y. L., Zhang, Q., Schwab, J. J., Yang, T., Ng, N. L., and Demerjian, K. L.: Factor analysis of combined organic and inorganic aerosol mass spectra from high resolution aerosol mass spectrometer measurements, Atmos. Chem. Phys., 12, 8537-8551, https://doi.org/10.5194/acp-12-8537-2012, 2012.

Topping, D. O., McFiggans, G. B., and Coe, H.: A curved multi-component aerosol hygroscopicity model framework: Part 2 – Including organic compounds, Atmos. Chem. Phys., 5, 1223-1242, https://doi.org/10.5194/acp-5-1223-2005, 2005a.

Topping, D. O., McFiggans, G. B., and Coe, H.: A curved multi-component aerosol hygroscopicity model framework: Part 1 – Inorganic compounds, Atmos. Chem. Phys., 5, 1205-1222, https://doi.org/10.5194/acp-5-1205-2005, 2005b.

Ulbrich, I. M., Canagaratna, M. R., Zhang, Q., Worsnop, D. R., and Jimenez, J. L.: Interpretation of organic components from Positive Matrix Factorization of aerosol mass spectrometric data, Atmos. Chem. Phys., 9, 2891-2918, https://doi.org/10.5194/acp-9-2891-2009, 2009.

Ulbrich, I. M., Canagaratna, M. R., Cubison, M. J., Zhang, Q., Ng, N. L., Aiken, A. C., and Jimenez, J. L.: Three-dimensional factorization of size-resolved organic aerosol mass spectra from Mexico City, Atmos. Meas. Tech., 5, 195-224, https://doi.org/10.5194/amt-5-195-2012, 2012.

Wang, J., Ge, X., Chen, Y., Shen, Y., Zhang, Q., Sun, Y., Xu, J., Ge, S., Yu, H., and Chen, M.: Highly time-resolved urban aerosol characteristics during springtime in Yangtze River Delta, China: insights from soot particle aerosol mass spectrometry, Atmos. Chem. Phys., 16, 9109-9127, https://doi.org/10.5194/acp-16-9109-2016, 2016.

Wang, J., Zhang, Q., Chen, M., Collier, S., Zhou, S., Ge, X., Xu, J., Shi, J., Xie, C., Hu, J., Ge, S., Sun, Y., and Coe, H.: First Chemical Characterization of Refractory Black Carbon Aerosols and Associated Coatings over the Tibetan Plateau (4730 m a.s.l), Environ. Sci. Technol., 51, 14072-14082, https://doi.org/10.1021/acs.est.7b03973, 2017.

1189   Wang, J., Liu, D., Ge, X., Wu, Y., Shen, F., Chen, M., Zhao, J., Xie, C., Wang, Q.,

1190   Xu, W., Zhang, J., Hu, J., Allan, J., Joshi, R., Fu, P., Coe, H., and Sun, Y.:

1191   Characterization of black carbon-containing fine particles in Beijing during wintertime,

1192   Atmos. Chem. Phys., 19, 447-458, https://doi.org/10.5194/acp-19-447-2019, 2019.

1193   Wang, J., Ye, J., Liu, D., Wu, Y., Zhao, J., Xu, W., Xie, C., Shen, F., Zhang, J.,

1194   Ohno, P. E., Qin, Y., Zhao, X., Martin, S. T., Lee, A. K. Y., Fu, P., Jacob, D. J., Zhang,

1195   Q., Sun, Y., Chen, M., and Ge, X.: Characterization of submicron organic particles in

1196   Beijing during summertime: comparison between SP-AMS and HR-AMS, Atmos.

1197   Chem. Phys., 20, 14091-14102, https://doi.org/10.5194/acp-20-14091-2020, 2020a.

1198   Wang, J., Ye, J., Zhang, Q., Zhao, J., Wu, Y., Li, J., Liu, D., Li, W., Zhang, Y., Wu,

1199   C., Xie, C., Qin, Y., Lei, Y., Huang, X., Guo, J., Liu, P., Fu, P., Li, Y., Lee, H. C., Choi,

1200   H., Zhang, J., Liao, H., Chen, M., Sun, Y., Ge, X., Martin, S. T., and Jacob, D. J.:

1201   Aqueous production of secondary organic aerosol from fossil-fuel emissions in winter

1202   Beijing haze, Proc. Natl. Acad. Sci. U. S. A., 118, e2022179118,

1203   https://doi.org/10.1073/pnas.2022179118, 2021.

1204   Wang, S., Newland, M. J., Deng, W., Rickard, A. R., Hamilton, J. F., Muñoz, A.,

1205   Ródenas, M., Vázquez, M. M., Wang, L., and Wang, X.: Aromatic Photo-oxidation, A

1206   New Source of Atmospheric Acidity, Environ. Sci. Technol., 54, 7798-7806,

1207   https://doi.org/10.1021/acs.est.0c00526, 2020b.

1208   Willis, M. D., Healy, R. M., Riemer, N., West, M., Wang, J. M., Jeong, C.-H.,

1209   Wenger, J. C., Evans, G. J., Abbatt, J. P. D., and Lee, A. K. Y.: Quantification of black

1210   carbon mixing state from traffic: implications for aerosol optical properties, Atmos.

1211   Chem. Phys., 16, 4693-4706, https://doi.org/10.5194/acp-16-4693-2016, 2016.

1212   Wu, Y., Ge, X., Wang, J., Shen, Y., Ye, Z., Ge, S., Wu, Y., Yu, H., and Chen, M.:

1213   Responses of secondary aerosols to relative humidity and photochemical activities in

1214   an industrialized environment during late winter, Atmos. Environ., 193, 66-78,

1215   https://doi.org/10.1016/j.atmosenv.2018.09.008, 2018.

1216   Wu, Y., Liu, D., Wang, J., Shen, F., Chen, Y., Cui, S., Ge, S., Wu, Y., Chen, M.,

1217   and Ge, X.: Characterization of Size-Resolved Hygroscopicity of Black Carbon-

1218   Containing Particle in Urban Environment, Environ. Sci. Technol., 53, 14212-14221,

1219 https://doi.org/10.1021/acs.est.9b05546, 2019.

1220 Wu, Y., Liu, D., Wang, X., Li, S., Zhang, J., Qiu, H., Ding, S., Hu, K., Li, W., Tian,
1221 P., Liu, Q., Zhao, D., Ma, E., Chen, M., Xu, H., Ouyang, B., Chen, Y., Kong, S., Ge, X.,
1222 and Liu, H.: Ambient marine shipping emissions determined by vessel operation mode
1223 along the East China Sea, Sci. Total Environ., 769, 144713,
1224 https://doi.org/10.1016/j.scitotenv.2020.144713, 2021.

1225 Wu, Z. J., Zheng, J., Shang, D. J., Du, Z. F., Wu, Y. S., Zeng, L. M., Wiedensohler,
1226 A., and Hu, M.: Particle hygroscopicity and its link to chemical composition in the
1227 urban atmosphere of Beijing, China, during summertime, Atmos. Chem. Phys., 16,
1228 1123-1138, https://doi.org/10.5194/acp-16-1123-2016, 2016.

1229 Xie, C., Xu, W., Wang, J., Liu, D., Ge, X., Zhang, Q., Wang, Q., Du, W., Zhao, J.,
1230 Zhou, W., Li, J., Fu, P., Wang, Z., Worsnop, D., and Sun, Y.: Light absorption
1231 enhancement of black carbon in urban Beijing in summer, Atmos. Environ., 213, 499-
1232 504, https://doi.org/10.1016/j.atmosenv.2019.06.041, 2019.

1233 Xu, J., Zhang, Q., Chen, M., Ge, X., Ren, J., and Qin, D.: Chemical composition,
1234 sources, and processes of urban aerosols during summertime in northwest China:
1235 insights from high-resolution aerosol mass spectrometry, Atmos. Chem. Phys., 14,
1236 12593-12611, https://doi.org/10.5194/acp-14-12593-2014, 2014.

1237 Xu, W., Han, T., Du, W., Wang, Q., Chen, C., Zhao, J., Zhang, Y., Li, J., Fu, P.,
1238 Wang, Z., Worsnop, D. R., and Sun, Y.: Effects of Aqueous-Phase and Photochemical
1239 Processing on Secondary Organic Aerosol Formation and Evolution in Beijing, China,
1240 Environ. Sci. Technol., 51, 762-770, https://doi.org/10.1021/acs.est.6b04498, 2017.

1241 Xu, W., Sun, Y., Wang, Q., Zhao, J., Wang, J., Ge, X., Xie, C., Zhou, W., Du, W.,
1242 Li, J., Fu, P., Wang, Z., Worsnop, D. R., and Coe, H.: Changes in Aerosol Chemistry
1243 From 2014 to 2016 in Winter in Beijing: Insights From High-Resolution Aerosol Mass
1244 Spectrometry, J. Geophys. Res.: Atmos., 124, 1132-1147,
1245 https://doi.org/10.1029/2018jd029245, 2019.

1246 Ye, Z., Liu, J., Gu, A., Feng, F., Liu, Y., Bi, C., Xu, J., Li, L., Chen, H., Chen, Y.,
1247 Dai, L., Zhou, Q., and Ge, X.: Chemical characterization of fine particulate matter in
1248 Changzhou, China, and source apportionment with offline aerosol mass spectrometry,

Atmos. Chem. Phys., 17, 2573-2592, https://doi.org/10.5194/acp-17-2573-2017, 2017.

Yu, G., Zhang, Y., Yang, F., He, B., Zhang, C., Zou, Z., Yang, X., Li, N., and Chen, J.: Dynamic Ni/V Ratio in the Ship-Emitted Particles Driven by Multiphase Fuel Oil Regulations in Coastal China, Environ. Sci. Technol., 55, 15031-15039, https://doi.org/10.1021/acs.est.1c02612, 2021.

Yu, L., Smith, J., Laskin, A., Anastasio, C., Laskin, J., and Zhang, Q.: Chemical characterization of SOA formed from aqueous-phase reactions of phenols with the triplet excited state of carbonyl and hydroxyl radical, Atmos. Chem. Phys., 14, 13801-13816, https://doi.org/10.5194/acp-14-13801-2014, 2014.

Zhang, F., Wang, Y., Peng, J., Chen, L., Sun, Y., Duan, L., Ge, X., Li, Y., Zhao, J., Liu, C., Zhang, X., Zhang, G., Pan, Y., Wang, Y., Zhang Annie, L., Ji, Y., Wang, G., Hu, M., Molina Mario, J., and Zhang, R.: An unexpected catalyst dominates formation and radiative forcing of regional haze, Proc. Natl. Acad. Sci. U. S. A., 117, 3960-3966, https://doi.org/10.1073/pnas.1919343117, 2020.

Zhang, G., Fu, Y., Peng, X., Sun, W., Shi, Z., Song, W., Hu, W., Chen, D., Lian, X., Li, L., Tang, M., Wang, X., and Bi, X.: Black Carbon Involved Photochemistry Enhances the Formation of Sulfate in the Ambient Atmosphere: Evidence From In Situ Individual Particle Investigation, J. Geophys. Res.: Atmos., 126, e2021JD035226, https://doi.org/10.1029/2021JD035226, 2021.

Zhang, Q., Canagaratna, M. R., Jayne, J. T., Worsnop, D. R., and Jimenez, J.-L.: Time- and size-resolved chemical composition of submicron particles in Pittsburgh: Implications for aerosol sources and processes, J. Geophys. Res., 110, https://doi.org/10.1029/2004JD004649, 2005.

Zhang, Q., Jimenez, J. L., Canagaratna, M. R., Ulbrich, I. M., Ng, N. L., Worsnop, D. R., and Sun, Y.: Understanding atmospheric organic aerosols via factor analysis of aerosol mass spectrometry: a review, Anal. Bioanal. Chem., 401, 3045-3067, https://doi.org/10.1007/s00216-011-5355-y, 2011.

Zhao, J., Qiu, Y., Zhou, W., Xu, W., Wang, J., Zhang, Y., Li, L., Xie, C., Wang, Q., Du, W., Worsnop, D. R., Canagaratna, M. R., Zhou, L., Ge, X., Fu, P., Li, J., Wang, Z., Donahue, N. M., and Sun, Y.: Organic Aerosol Processing During Winter Severe Haze

1279 Episodes in Beijing, J. Geophys. Res.: Atmos., 124, 10248-10263,
1280 https://doi.org/10.1029/2019jd030832, 2019.

1281   Zhao, M., Zhang, Y., Ma, W., Fu, Q., Yang, X., Li, C., Zhou, B., Yu, Q., and Chen,
1282 L.: Characteristics and ship traffic source identification of air pollutants in China's
1283 largest   port,   Atmos.   Environ.,   64,   277-286,
1284 https://doi.org/10.1016/j.atmosenv.2012.10.007, 2013.

1285   Zhou, S., Collier, S., Xu, J., Mei, F., Wang, J., Lee, Y.-N., Sedlacek, A. J.,
1286 Springston, S. R., Sun, Y., and Zhang, Q.: Influences of upwind emission sources and
1287 atmospheric processing on aerosol chemistry and properties at a rural location in the
1288 Northeastern   U.S,   J.   Geophys.   Res.:   Atmos.,   121,   6049-6065,
1289 https://doi.org/10.1002/2015jd024568, 2016.

1290
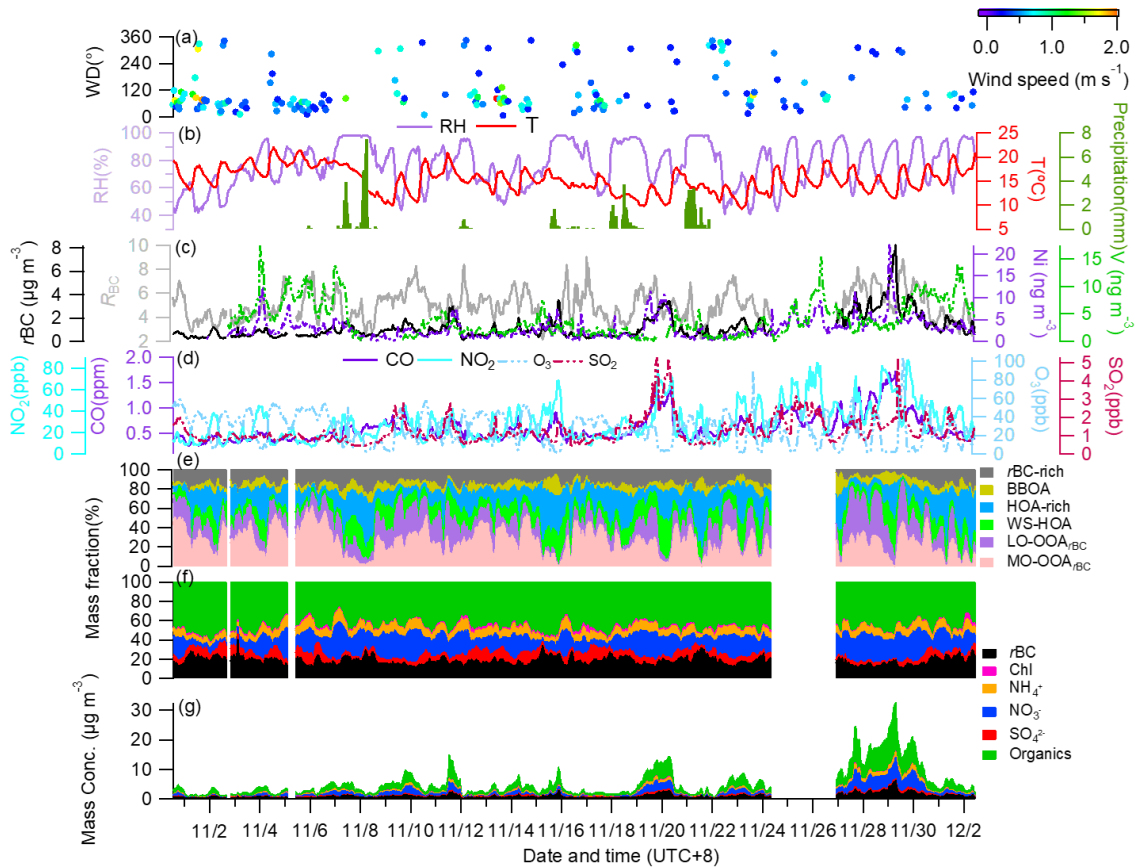
1291

Figure 1. Time series of (a) wind direction (WD) colored by wind speed (WS), (b) air
temperature (T), relative humidity (RH) and precipitation, (c) mass concentrations of
rBC, Ni, V, and R_{BC} (mass ratio of all coating species to rBC), (d) mass concentrations
of gas pollutants of CO, NO_2, O_3 and SO_2, (e) mass fractions (%) of different OA factors
to the total rBCc OA, (f) mass fractions (%) of different components to the total rBCc
mass, and (g) mass concentrations of stacked rBCc components.
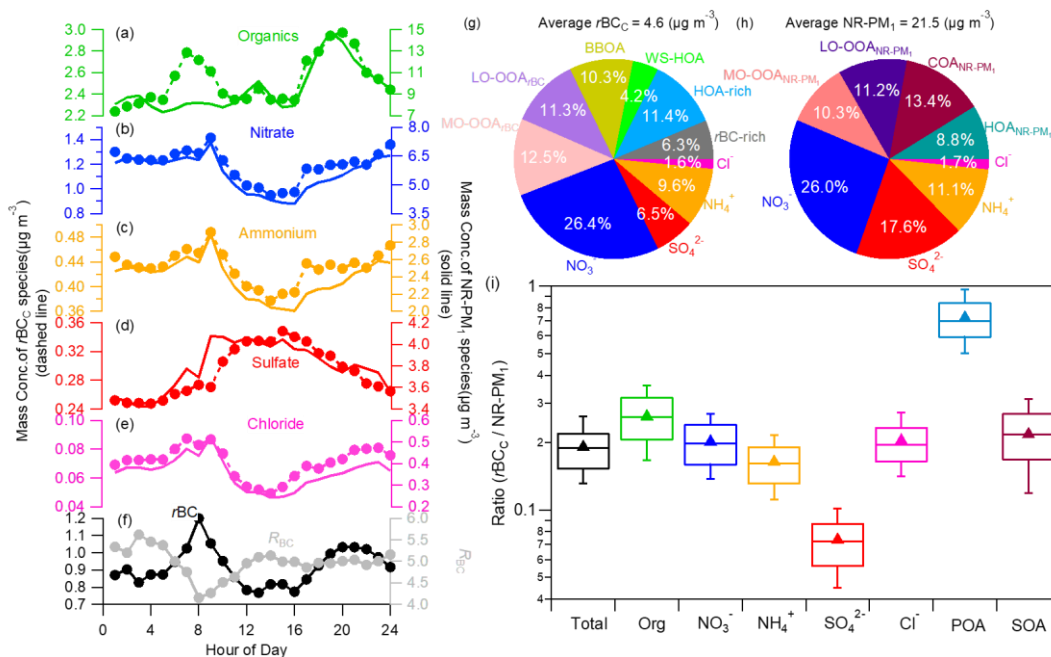
1298

Figure 2. Diurnal cycles of mass concentrations of (a–e) rBCc and NR-PM$_1$ species (organics, nitrate, ammonium, sulfate, and chloride), and (f) rBC and R_{BC}. Campaign-average chemical composition of rBCc (g) and NR-PM$_1$ (h). (i) Mass ratios of species in rBCc to those in NR-PM$_1$ (the whiskers above and below the boxes mark the 90% and 10% percentiles, respectively; the upper and lower edge of the boxes represent the 75% and 25% percentiles, respectively; and the lines and triangles inside the boxes denote the median and mean values, respectively; SOA represents ([LO-OOA$_{rBC}$] + [MO-OOA$_{rBC}$])/([LO-OOA$_{NR-PM1}$] + [LV-OOA$_{NR-PM1}$]), and POA represents ([rBC-rich + HOA-rich + BBOA + WS-HOA])/HOA$_{NR-PM1}$).
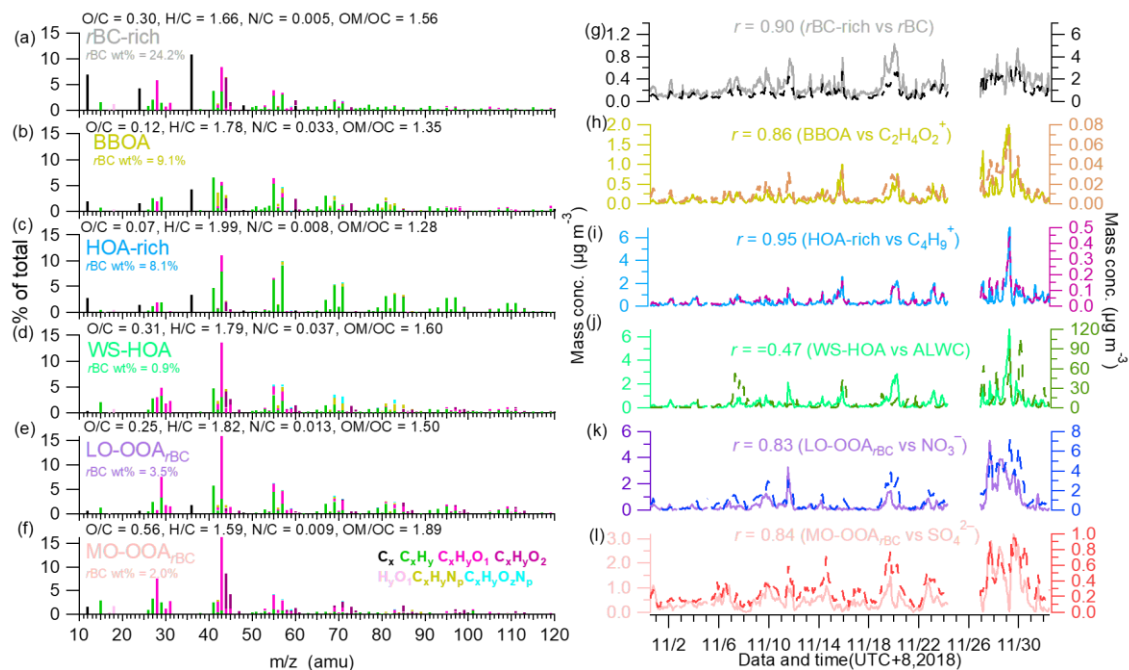
1308

1309 Figure 3. High resolution mass spectra of (a) rBC-rich, (b) BBOA, (c) HOA-rich, (d)

1310 WS-HOA, (e) LO-OOA$_{r\text{BC}}$, and (f) MO-OOA$_{r\text{BC}}$. (g-l) Time series of corresponding

1311 factors, their tracers (rBC, $C_2H_4O_2^+$, $C_4H_9^+$, ALWC, nitrate and sulfate) as well as the

1312 correlation coefficients (ALWC refers to aerosol liquid water content, which was

1313 estimated by using the model II of extended aerosol inorganic model (E-AIM II)(Clegg

1314 et al., 1998); calculation details and results at different RH values are described in the

1315 caption and shown in Fig. S6)

1316
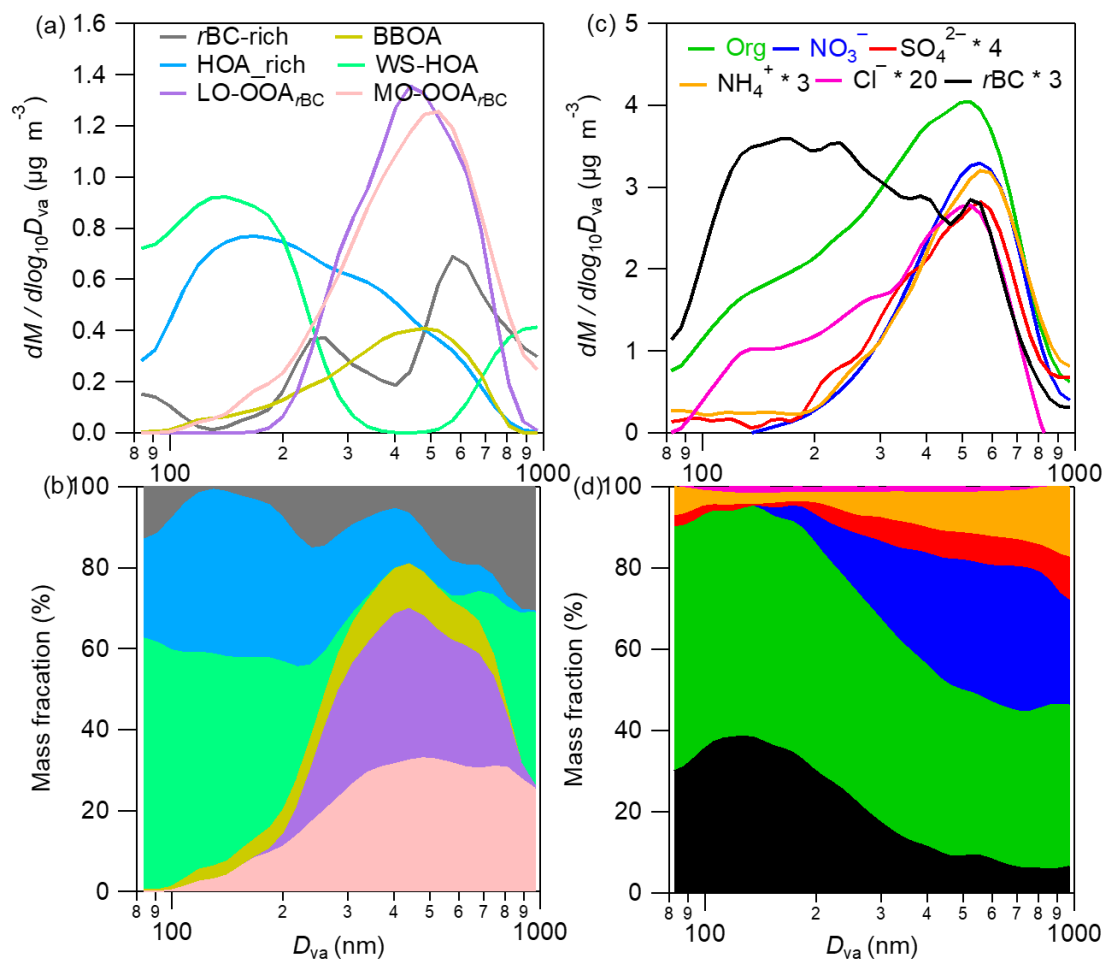
1317

1318 Figure 4. Campaign-average size distributions of six *r*BCc OA factors (a) and individual

1319 *r*BCc components (b), and corresponding mass contributions of the six factors to the

1320 total *r*BCc OA (c), and the major components to the total *r*BCc (d) at different sizes

1321 (80-1000 nm).

1322

1323
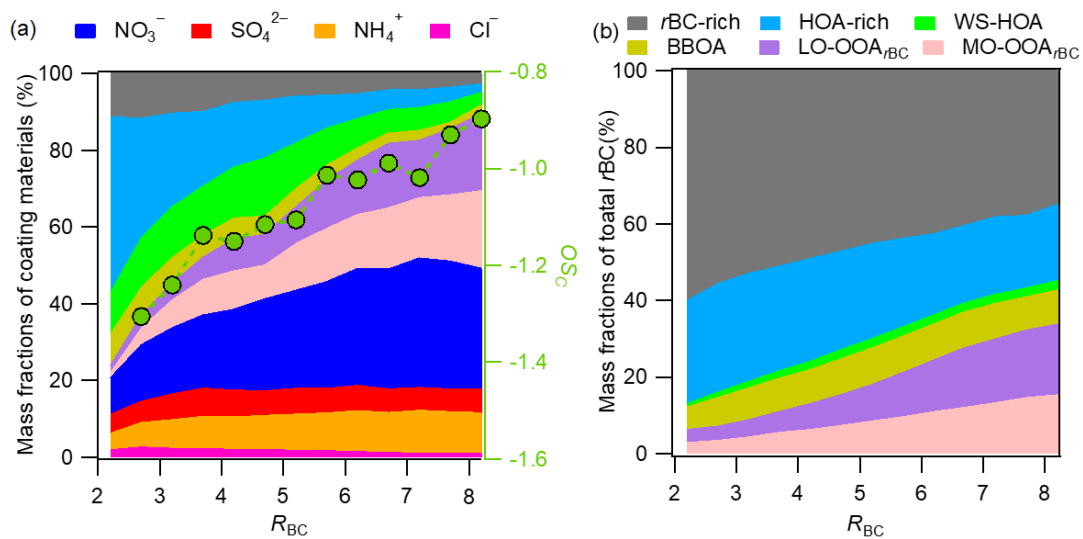
1324

1325   Figure 5. (a) Variations of mass fractions of the major rBCc components against R_{BC}.

1326   (b) Variations of mass contributions of individual rBCc OA factors to rBC against R_{BC}.

1327
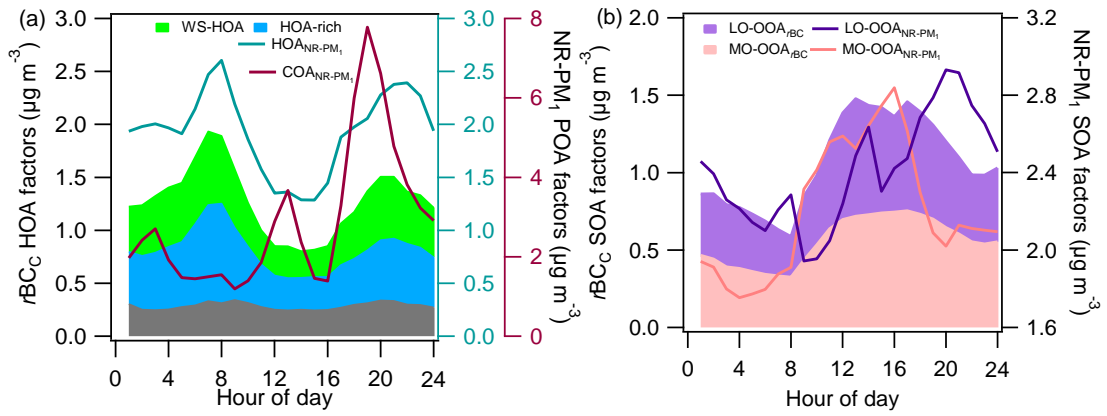
1328

1329 Figure 6. Comparisons of the diurnal patterns of different POA factors (b) and SOA

1330 factors (c) of rBCc and NR-PM$_1$.

1331

1332
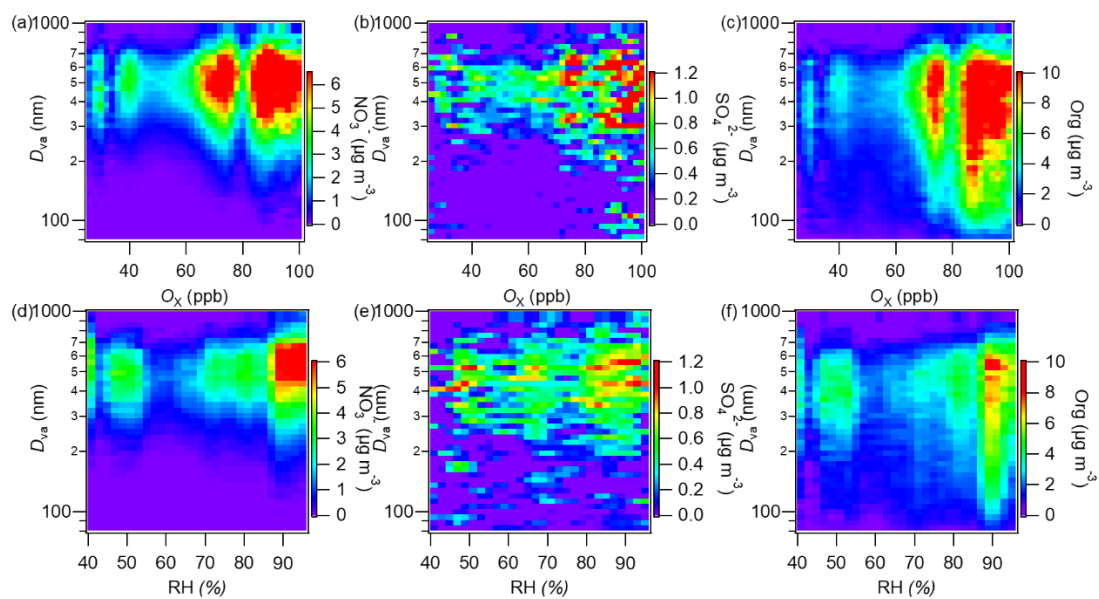
1333

1334   Figure 7. Image plots of size distributions of rBCc nitrate, sulfate, organics as a function

1335   of (a-c) O_X and (d-f) RH, respectively (color represents its concentration).

1336
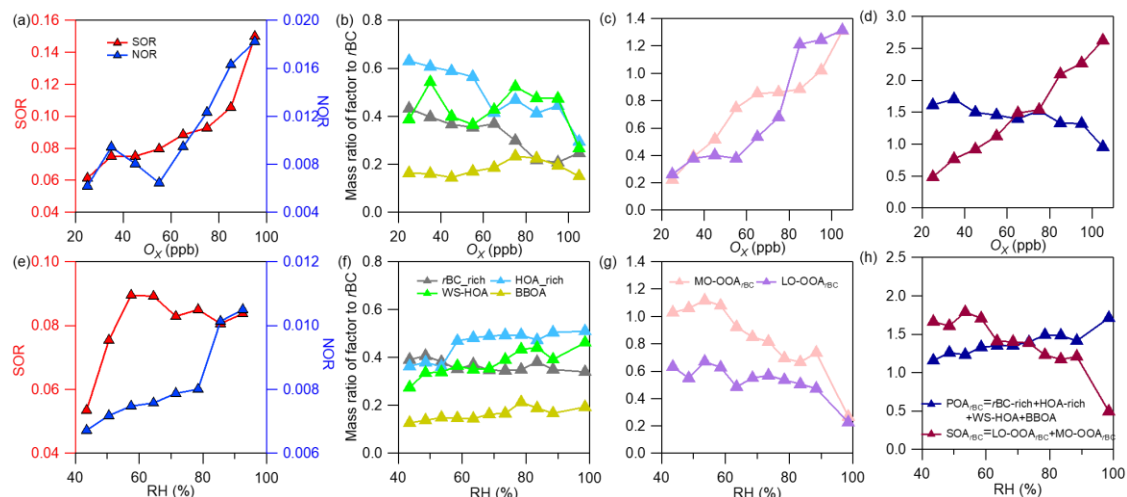
1337

Figure 8. Variations of nitrogen oxidation ratio (NOR) and sulfur oxidation ratio, mass ratios of different POA factors, SOA factors and total POA and SOA to rBC against O_X (a-d) and RH (e-h) (NOR= $n\text{NO}_3^-/(n\text{NO}_3^-+n\text{NO}_2+n\text{NO})$ and SOR= $n\text{SO}_4^{2-}/(n\text{SO}_4^{2-}+n\text{SO}_2)$, where $n\text{NO}_3^-$, $n\text{SO}_4^{2-}$, $n\text{NO}_2$, $n\text{NO}$ and $n\text{SO}_2$ are the molar concentrations of particle-phase sulfate, nitrate, gaseous NO₂, NO and SO₂, respectively).

1343
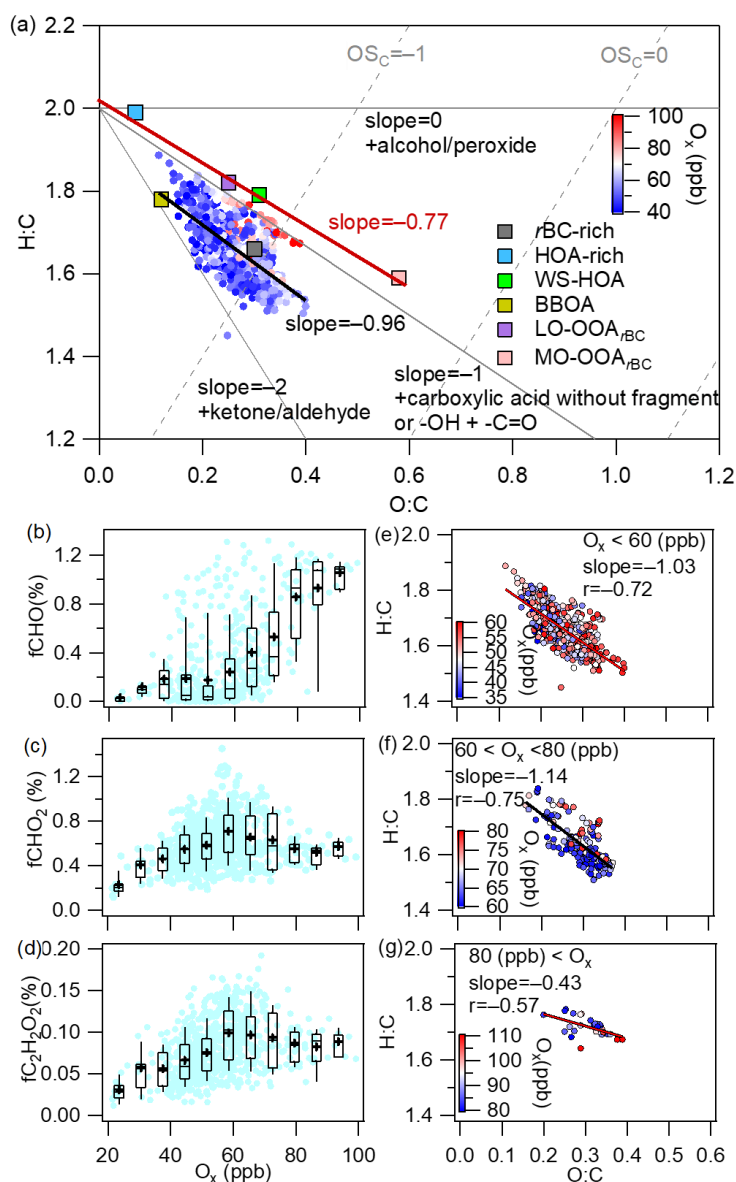
1344

Figure 9. (a) Van Krevelen diagram of H/C versus O/C ratios for all *r*BCc OA and the

six factors colored by Oₓ concentrations (the black line represents the linearly fitted

line of all OA data, and the red line is the fitted line of the four OA factors). (b-d) Mass

fractions of selected oxygenated ion fragments as a function of Oₓ (meanings of the

boxes are the same as those described in Fig. 2). (e-g) Scatter plots of H/C versus O/C

ratios under different Oₓ levels (data are colored by Oₓ concentrations).
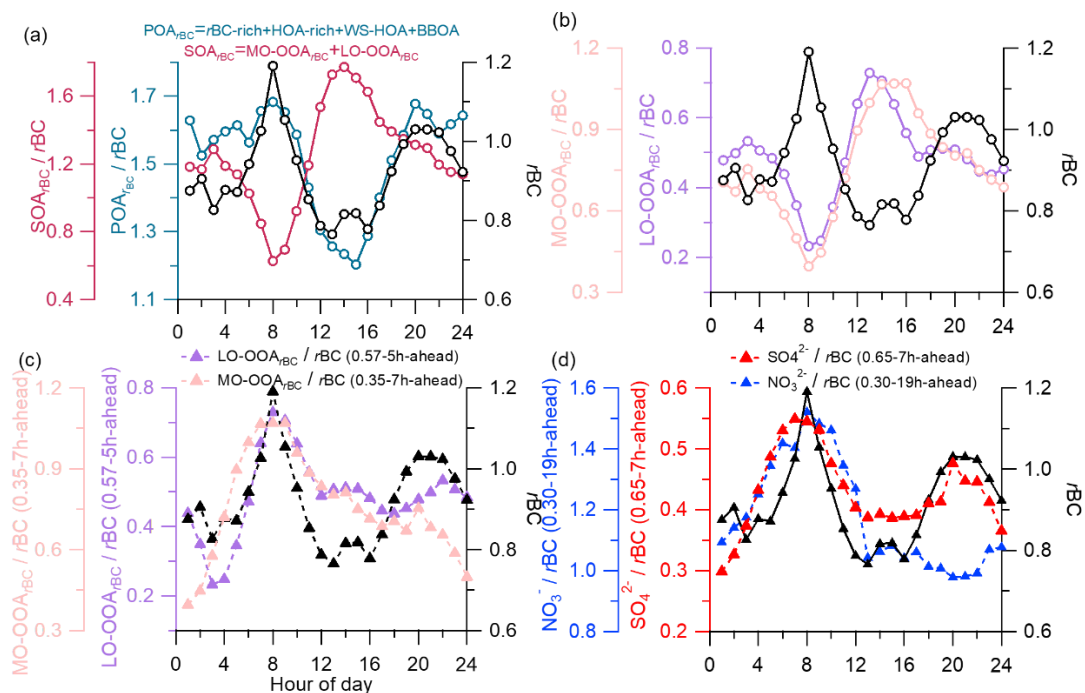
Figure 10. Campaign-average diurnal patterns of (a) rBC, POA$_{r\text{BC}}$/rBC and SOA$_{r\text{BC}}$/rBC, and (b) rBC, MO-OOA$_{r\text{BC}}$/rBC and LO-OOA$_{r\text{BC}}$/rBC. Adjusted diurnal patterns by the average coating time (ACT) for (c) LO-OOA$_{r\text{BC}}$/rBC, MO-OOA$_{r\text{BC}}$/rBC, and (d) SO$_4^{2-}$/rBC, NO$_3^-$/rBC.
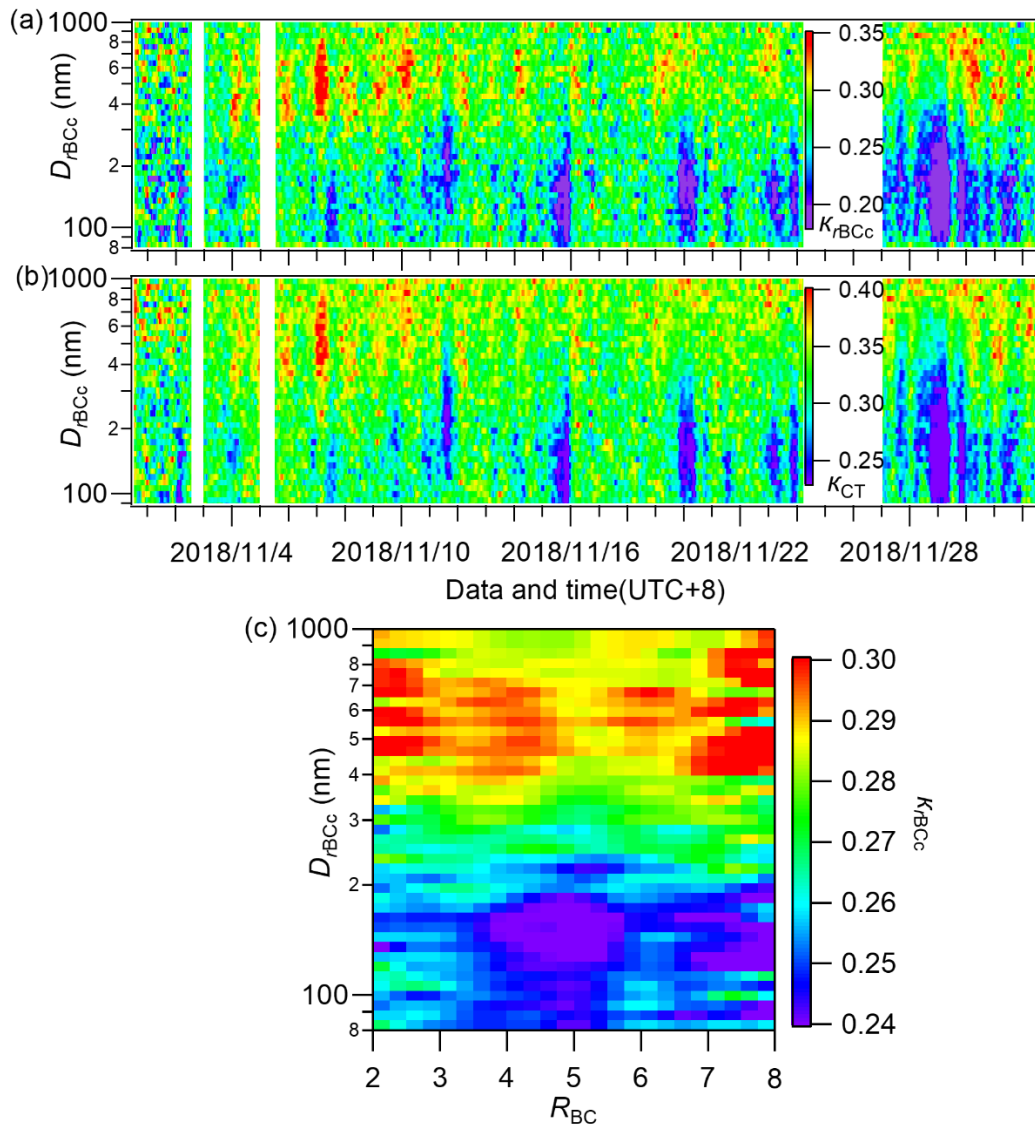
Figure 11. Image plots of size-resolved hygroscopicity parameters of (a) rBCc ($\kappa_{r\text{BCc}}$), (b) its coating materials (κ_{CT}) during the whole campaign, and (c) the campaign-average size-resolved $\kappa_{r\text{BCc}}$ at different R_{BC}.
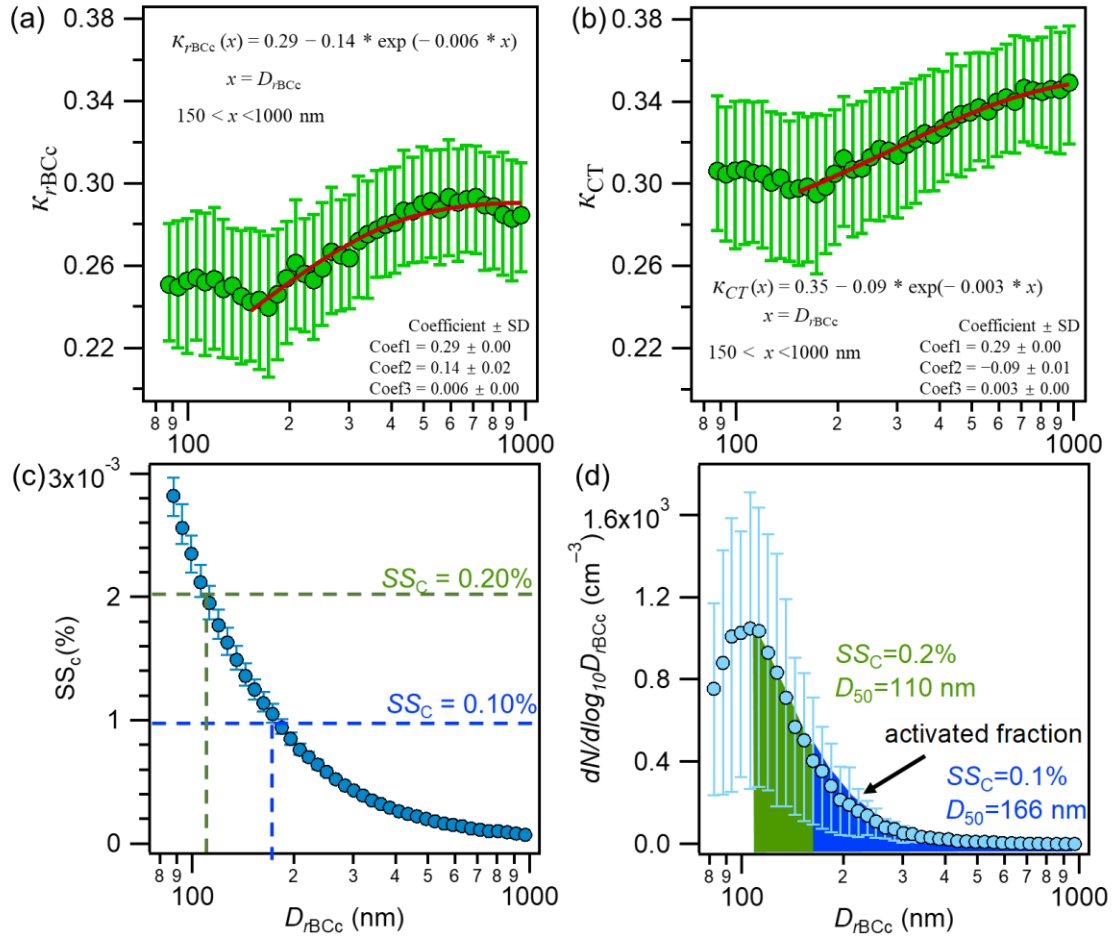
Figure 12. Campaign-average size-resolved hygroscopic parameters for rBCc ($\kappa_{r\mathrm{BCc}}$) and (a) for its coatings (κ_{CT}) (b) (the red lines are exponential fits of the data of 150-1000 nm). (c) Campaign-average size-resolved critical supersaturation (SS_C), and (d) the predicted activated fraction of rBCc number concentration based on D_{50} at SS_C of 0.1% (166 nm) and 0.2% (110 nm) (the solid circles are mean values, the upper and lower lines are the 75th and 25th percentiles, respectively).

1369
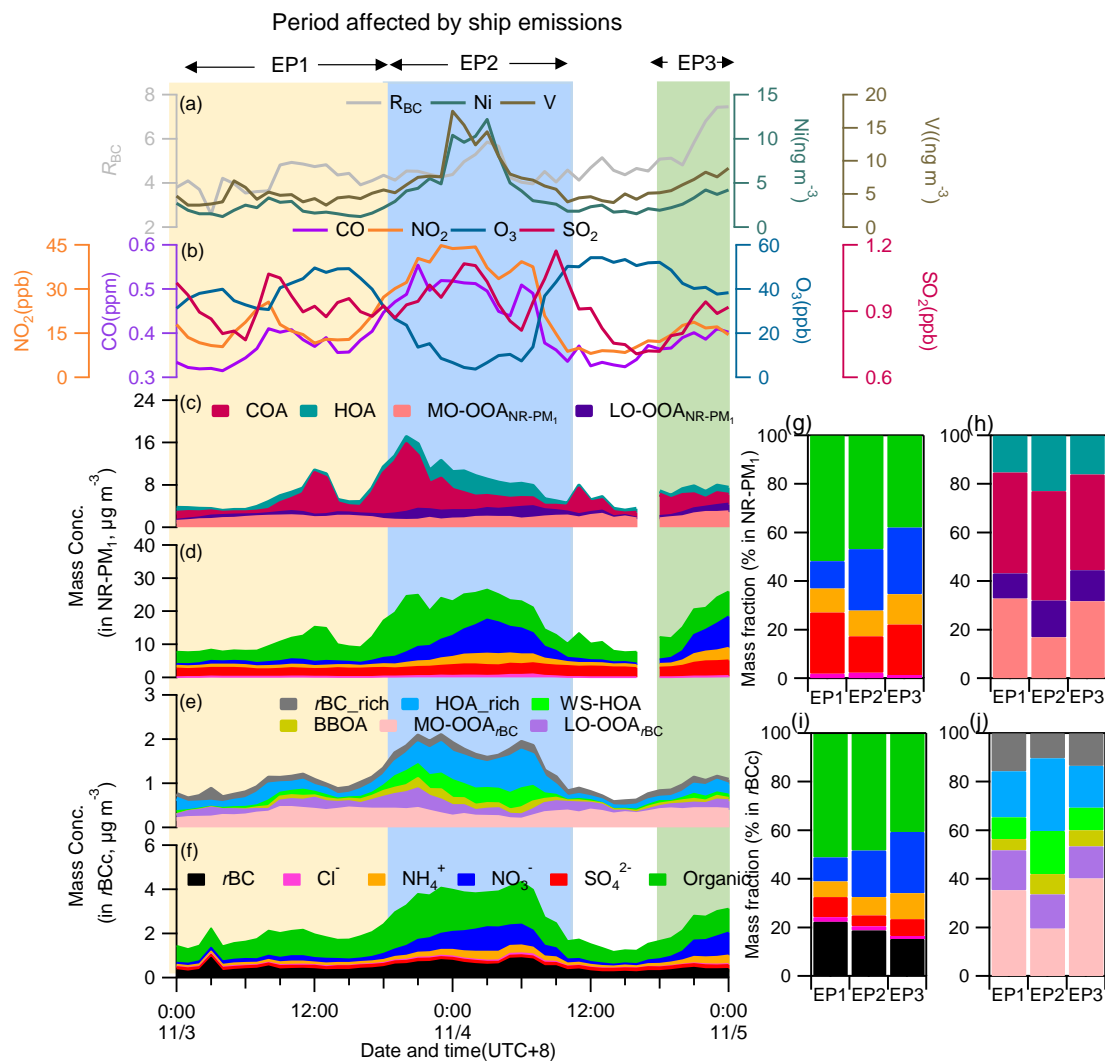
Figure 13. Time series of (a) mass concentrations of particle-phase Ni and V, and R_{BC},

(b) mass concentrations of CO, NO$_2$, O$_3$, SO$_2$, stacked concentrations of (c) NR-PM$_1$

OA factors, (d) NR-PM$_1$ species, (e) rBCc OA factors, and (f) rBCc components during

the ship emission period (SEP). Mass contributions of (g) different components to NR-

PM$_1$, (h) different OA factors to total NR-PM$_1$ OA, (i) different components to rBCc,

and (j) different OA factors to total rBCc OA for the three episodes (EP1, EP2 and

EP3).

1377